Dipole response in ^{128,130}Te below the neutron threshold

J. Isaak,[1,*] D. Savran,[2] B. Löher,[2] T. Beck,[1] U. Friman-Gayer,[1,3,4] Krishichayan,[5,3] N. Pietralla,[1] V. Yu. Ponomarev,[1] M. Scheck,[6,7] W. Tornow,[5,3] V. Werner,[1] A. Zilges,[8] and M. Zweidinger[1]

[1]*Institut für Kernphysik, Technische Universität Darmstadt, Schlossgartenstrasse 9, 64289 Darmstadt, Germany*
[2]*GSI Helmholtzzentrum für Schwerionenforschung GmbH, Planckstrasse 1, 64291 Darmstadt, Germany*
[3]*Triangle Universities Nuclear Laboratory, Durham, North Carolina 27708-0308, USA*
[4]*Department of Physics and Astronomy, University of North Carolina at Chapel Hill, Chapel Hill, North Carolina 27599, USA*
[5]*Department of Physics, Duke University, Durham, North Carolina 27708-0308, USA*
[6]*School of Computing, Engineering, and Physical Sciences, University of the West of Scotland, Paisley, PA1 2BE, United Kingdom*
[7]*SUPA, Scottish Universities Physics Alliance, United Kingdom*
[8]*Institut für Kernphysik, Universität zu Köln, Zülpicher Strasse 77, 50937 Köln, Germany*

(Received 7 January 2021; accepted 11 March 2021; published 22 April 2021)

Background: Numerous studies of the ground-state decay of the pygmy dipole resonance (PDR) have been carried out in the past. However, data on the decay of the PDR to low-lying excited states is still very scarce due to limitations of the sensitivity to weak branching transitions of experimental setups.
Purpose: We present a detailed examination of the low-energy dipole response of ^{128}Te and ^{130}Te below their neutron separation thresholds of 8.8 and 8.5 MeV, respectively.
Methods: Photonuclear reactions with the subsequent γ-ray spectroscopy of the decay channel with continuous-energy bremsstrahlung at varying endpoint energies and linearly polarized quasimonochromatic γ-ray beams with energies ranging from 2.7 to 8.9 MeV in steps of roughly 250 keV were used for probing the decay behavior of the low-energy dipole response in ^{128}Te and ^{130}Te. In addition, $(\vec{\gamma}, \gamma'\gamma'')$ reactions were used to study the population of low-lying states of ^{128}Te.
Results: Spin-parity quantum numbers and reduced transition probabilities are determined for individual photo-excited states. The analysis of average decay properties for nuclear levels in narrow excitation-energy bins enable the extraction of photoabsorption cross sections, average branching ratios to the 2_1^+ state, and the distinction between $E1$ and $M1$ transitions to the ground state and to the 2_1^+ state accounting for resolved and unresolved transitions.
Conclusions: Above 5 MeV, the experimental data are in reasonable agreement to calculations within the quasiparticle phonon model. The major fraction of the ground-state decay channel is due to $E1$ transitions, while less than 5–10% stem from $M1$ transitions. Furthermore, first direct experimental evidence is provided that the population of the 2_1^+ state of ^{128}Te via primary γ-ray transitions from excited states in the PDR region from 5 to 9 MeV is dominated by $E1$ transitions of 1^- states.

DOI: 10.1103/PhysRevC.103.044317

I. INTRODUCTION

The investigation of nuclear excitation modes is one of the major approaches in low-energy nuclear physics research to explore fundamental properties of the atomic nucleus such as the single-particle structure or bulk properties of nuclear matter. One of the prominent excitation modes is the well-known isovector giant dipole resonance (IVGDR). It was first observed by Bothe and Gentner [1] in 1937 and systematically studied by Baldwin and Klaiber [2]. Extensive experimental and theoretical efforts over the past decades lead to a profound understanding of the IVGDR [3,4], which is macroscopically interpreted as a collective out-of-phase dipole oscillation of all protons against all neutrons of a heavy nucleus [5]. The observation of a concentration of dipole strength in the vicinity of the particle thresholds on top of the low-energy tail of the IVGDR [6,7] triggered a variety of experimental attempts to unravel its structure and origin. Over the past decades, the additional dipole strength was assigned an electric dipole ($E1$) character and is nowadays often denoted as pygmy dipole resonance (PDR); see Refs. [8–10] for recent reviews of experimental results and theoretical methods. Most microscopic models predict the PDR simultaneously to the IVGDR in the $E1$ response of the nucleus. Despite extensive research, the nature of the PDR is still unclear and highly debated. In a geometrical picture it was first interpreted as an out-of-phase oscillation of the isospin-saturated core against a neutron skin generated by the excess neutrons [11]. This is nowadays further motivated by an investigation of associated transition densities within modern microscopic models (for an overview see, e.g., Refs. [9,12] and references therein). Amongst others,

*jisaak@ikp.tu-darmstadt.de

an alternative interpretation of the low-energy 1^- states is by virtue of a dipole toroidal excitation mode [13] that is linked to a confined vortical flow within the nucleus (see, e.g., Ref. [14]).

One of the consequences of the enhanced $E1$ strength in the PDR region is its role in the synthesis of heavy elements. Due to its location in the vicinity of the particle thresholds, it has an impact on predictions of the nucleosynthesis and neutron capture reaction rates [15–19] in astrophysical network calculations. Moreover, the study of the low-lying $E1$ strength is important for refining models of photon strength functions (see, e.g., Refs. [20–30] and references therein for different experimental methods), which are one of the basic input quantities in Hauser-Feshbach calculations [31] performed by statistical model codes such as TALYS [32] and EMPIRE [33].

Systematic experimental investigations of the low-energy dipole strength were conducted with electromagnetic probes, particularly in nuclei located at major shell closures. Throughout the nuclear chart, an enhancement of $E1$ strength was observed on top of the IVGDR low-energy tail, e.g., in the stable Ca [34,35] and Cr [36–38] isotopes as well as stable [39,40] and unstable [41–43] Ni isotopes. Furthermore, the $E1$ strength was studied in the $N = 82$ isotones [44–47] and along the Sn ($Z = 50$) isotopic chain in stable (see, e.g., Refs. [48–54]) and unstable isotopes [55,56], in the Mo isotopes [57–60] as well as in heavy nuclei such as ^{206,208}Pb [19,61,62].

Studies using complementary probes have been performed to investigate the properties of the PDR in more detail. Exploiting the $(\alpha, \alpha'\gamma)$ [49,63–65] and $(^{17}\mathrm{O}, ^{17}\mathrm{O}'\gamma)$ [9,66,67] reactions revealed a structural splitting of the observed low-lying $E1$ strength in numerous nuclei. The combination of such complementary data has opened the possibility to a detailed examination of the PDR in comparison to nuclear models [65]. Recently, also β-decay into states of the PDR [68,69] as well as the determination of the decay behavior [39,47] were added to the portfolio of experimental observables. For a more comprehensive summary of experimental data on the PDR see Refs. [8–10].

In this work, we present an extended study of low-energy $E1$ excitations in the PDR region of ^{128,130}Te using nuclear resonance fluorescence (NRF) reactions [70–72] at the γ^3 setup [73] taking advantage of its sensitivity for decay branchings on the few-percent level. The tellurium isotopes ($Z = 52$) serve as a good case to extend the systematic analysis to regions on the nuclear chart apart from shell closures to study more complex configurations, e.g., the influence of two valence protons on the evolution of the PDR strength as a function of the neutron excess. Besides the extraction of the full dipole strength and its multipole character, the data allow for the analysis of primary γ-ray transitions to low-lying excited states exploiting the combination of quasimonochromatic γ-ray beams and the γ-γ coincidence technique [27,47]. In addition, data from NRF experiments with continuous-energy bremsstrahlung are presented.

The article is organized as follows. After a brief summary of the experimental details, the data analysis of the NRF experiments with bremsstrahlung and quasimonochromatic γ-ray beams will be presented. This is followed by a discussion of the results from a state-by-state analysis and from an analysis of average quantities in comparison to calculations with the quasiparticle phonon model (QPM) [74]. Before the manuscript is concluded, a detailed examination of the decay properties of the PDR in ^{128}Te extracted from γ-γ correlations is conducted. The data shown and discussed in this article are tabulated in the Supplemental Material [75] partly using information and decay properties of already known levels from Refs. [76–80].

II. EXPERIMENT

The low-lying dipole strength in ^{128}Te and ^{130}Te is investigated in photon-scattering experiments at two experimental facilities. One set of experiments was performed at the Darmstadt high-intensity photon setup (DHIPS) [81] using continuous-energy bremsstrahlung. Photons are produced via bremsstrahlung by stopping the electron beam delivered by the injector of the superconducting Darmstadt electron linear accelerator (S-DALINAC) [82] in different radiator materials. In the experiments with ^{128}Te silver and gold material were irradiated for the bremsstrahlung production with endpoint energies of 6 and 9.13 MeV, respectively, while a copper radiator was used for the ^{130}Te measurements with electron kinetic energies of 6.4 and 8.5 MeV. Collimated by a copper collimator of about 2.5 cm diameter the continuous photon beam impinges on the scattering target. Three large volume high-purity germanium (HPGe) detectors with 100% relative photopeak efficiency (relative to an NaI detector of 7.6 cm in length and 7.6 cm in diameter at a γ-ray energy of 1.3 MeV) are placed close to the target to detect the emitted γ rays at different scattering angles of 90° and 130° with respect to the photon-beam direction. The HPGe detectors are shielded with copper and lead to suppress low-energy background radiation and are equipped with bismuth germanate (BGO) active Compton-suppression shields, that considerably improve the peak-to-background ratio in the experimental γ-ray spectra [83].

The second measurement was conducted at the High Intensity γ-ray Source (HIγS) [84]. The HIγS facility provides fully linearly polarized and quasimonochromatic photon beams, that are generated via intracavity laser Compton backscattering of relativistic electrons and free-electron laser (FEL) photons. The experimental setup is located approximately 60 m downstream from the collision point of the FEL photons and the electron beam. The γ-ray beam is collimated by a copper and lead collimator of 1.9 cm in diameter before it impinges the scattering target and exhibits a bandwidth of $\Delta E/E \approx 3$–4% [84].

Two different detector setups were used at HIγS for the measurements with ^{128}Te and ^{130}Te, respectively. The experiments with ^{128}Te were performed at the γ^3 setup [73]. This setup consists of two types of detectors: (a) four HPGe detectors (60% relative photopeak efficiency) and (b) four $LaBr_3$:Ce scintillators with a crystal size of $3'' \times 3''$. The target was centered between the detectors, that were placed at different polar scattering angles (ϑ) and azimuthal (φ) angles, which are defined as the angle between the reaction plane and the polarization plane, respectively. The high efficiency

TABLE I. Summary of target information and γ-ray beam energies for the experiments performed with ^{128}Te and ^{130}Te.

	^{128}Te	^{130}Te
Target mass (mg)	2912.8(5)	1998.0(5)
Isotopic enrichment (%)	99.8	99.5
Physical form	Metallic	Metallic
DHIPS endpoint energies (MeV)	6.0 & 9.13	6.4 & 8.5
HIγS beam energies (MeV) in steps of 150–350 keV	2.76–8.92	5.5–8.5

of this setup allows to perform γ-γ coincidence spectroscopy providing the possibility to investigate the decay properties of photoexcited states with high sensitivity [27,47,85,86].

For the NRF measurements with ^{130}Te a reduced setup was used. Four HPGe detectors were positioned in a cross-like geometry perpendicular to the photon beam at different azimuthal angles. No data from γ-γ coincidence spectroscopy are available for this isotope in the present analysis.

Details on the targets and the photon beam energies are given in Table I, while the individual detector positions for both setup geometries for the measurements at HIγS are summarized in Table II.

The combination of the measurements at both experimental setups (DHIPS and γ^3 setup) allows the assignment of spin and parity-quantum numbers of nuclear levels as well as the determination of absolute scattering cross sections in a state-by-state analysis and averaged in small excitation-energy bins, respectively.

III. DATA ANALYSIS

In the following, the data analysis of the experiments with ^{128}Te and ^{130}Te will be discussed. Differences in the analysis of both isotopes due to the different setups are described in the text when necessary.

In the thin-target approximation of NRF reactions, the measured peak area $A_{0\to x\to i}$ corresponding to the photo-excitation of an initial excited state x from the ground state and the subsequent deexcitation to a final state i is given by

$$A_{0\to x\to i} = N_T\, N_\gamma(E_x)\, I_{0\to x\to i} \times \int_{\Delta\Omega} d\Omega\, \varepsilon(E_x - E_i, \Omega)\, W_{0\to x\to i}(\Omega), \quad (1)$$

TABLE II. Summary of detector positions used in the experiments at HIγS with ^{128}Te and ^{130}Te.

^{128}Te		^{130}Te
HPGe (ϑ, φ)	$LaBr_3$:Ce (ϑ, φ)	HPGe (ϑ, φ)
(90°, 180°)	(90°, 0°)	(90°, 0°)
(90°, 270°)	(90°, 90°)	(90°, 90°)
(135°, 225°)	(135°, 45°)	(90°, 180°)
(135°, 315°)	(135°, 135°)	(90°, 270°)

with N_T and N_γ being the number of target nuclei and the photon flux, respectively, while $I_{0\to x\to i}$ corresponds to the energy-integrated scattering cross section. The photopeak efficiency $\varepsilon(E_x - E_i, \Omega)$ varies depending on the position and angle of the emitted photons relative to the detector surface. The angular distribution of the emitted photons is given by $W_{0\to x\to i}(\Omega)$. The integration over the solid angle $\Delta\Omega$ takes the finite dimensions of the detector and the target into account.

Figure 1 shows the γ-ray spectra obtained at DHIPS at a scattering angle of $\vartheta = 130^\circ$ with respect to the incoming beam with endpoint energies of $E_{e^-} = 9.13$ MeV and $E_{e^-} = 8.5$ MeV for ^{128}Te and ^{130}Te, respectively. The majority of the γ transitions stem from photo-excited states in ^{128,130}Te except for a few pronounced peaks assigned to transitions in ^{11}B which is used as a calibration standard. Below the neutron-emission thresholds of $S_n(^{128}\text{Te}) = 8.78$ MeV and $S_n(^{130}\text{Te}) = 8.4$ MeV an accumulation of transitions are clearly observed in the region between 5.5 and 8 MeV. In the case of ^{130}Te a significant amount of the total intensity is located in large isolated peaks in contrast to ^{128}Te, where the strength is more fragmented.

The energy-integrated scattering cross section for the decay to a final state i after photo-excitation to an excited state x is connected to the partial transition width to the ground state and to the final state i, Γ_0 and Γ_i, respectively, as well as to the total transition width $\Gamma = \sum_i \Gamma_i$ of an excited state at E_x:

$$I_{0\to x\to i} = \pi^2 \left(\frac{\hbar c}{E_x}\right)^2 g \frac{\Gamma_0 \Gamma_i}{\Gamma}, \quad (2)$$

where the statistical factor $g = (2J_x + 1)/(2J_0 + 1)$ is expressed by the spin-quantum number of the excited state J_x and the ground state J_0, respectively. This model independent and analytical connection of the measured cross section to the transition width of excited states is one of the major advantages of the NRF reaction.

A. Photon-flux calibration

In NRF experiments using continuous-energy bremsstrahlung the integrated cross sections are usually determined relative to a calibration standard which is measured simultaneously to the nucleus of interest. In the present case, ^{11}B is used as calibration target, which has several strongly excited states between 2 and 9 MeV (see Fig. 1) with well-known energy-integrated scattering cross sections [87]. This procedure was described in detail in numerous works before (see, e.g., Ref. [88]).

A different approach for the photon-flux calibration is often used in experiments with quasimonochromatic photon beams at HIγS. Using ^{11}B as calibration standard to determine integrated scattering cross sections of individual excited states is not feasible at HIγS due to the quasimonochromatic character of the photon beam. In most cases, the corresponding level energies in ^{11}B do not coincide with the photon beam energies chosen for the measurement with ^{128}Te and ^{130}Te. The alternative approach is exemplarily illustrated in Fig. 2 for two photon beam energies of $E_b = 6.19$ MeV and 7.72 MeV using ^{128}Te. The spectral distribution of the incident photon beam is measured with a 123% HPGe detector placed into the

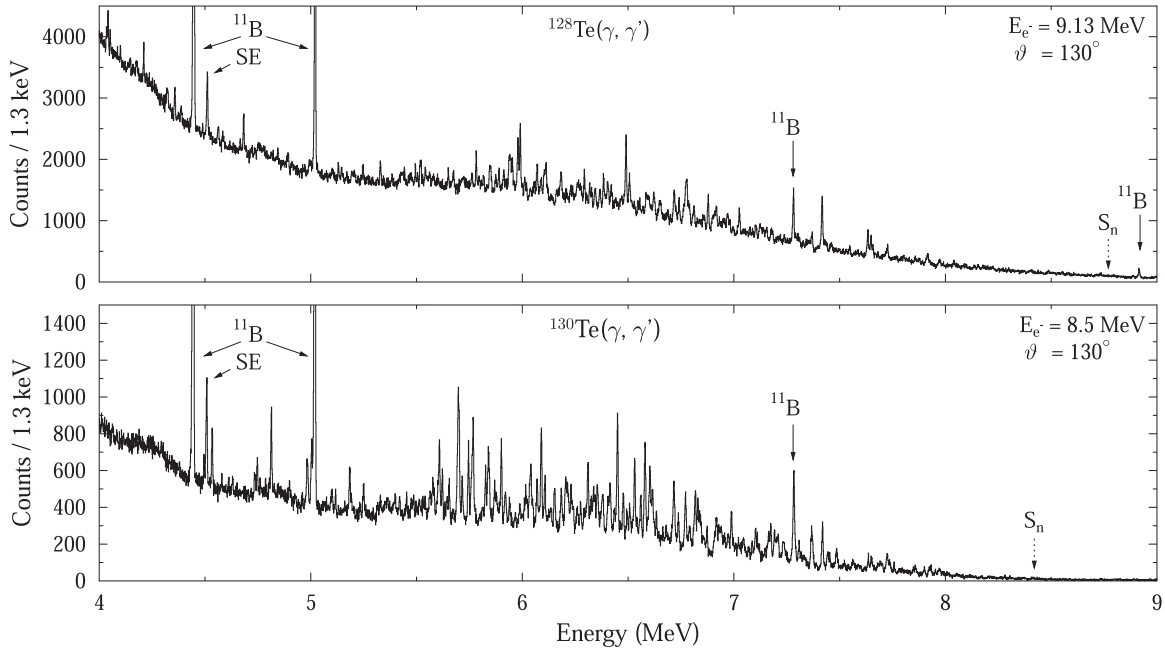

FIG. 1. Measured γ-ray spectra at an azimuthal scattering angle of $\vartheta = 130^\circ$ at DHIPS for ^{128}Te (upper panel) and ^{130}Te (lower panel) with electron beam energies of $E_{e^-} = 9.13$ MeV and $E_{e^-} = 8.5$ MeV, respectively. Peaks originating from transitions of the calibration standard ^{11}B and the single escape (SE) peak of the 5020-keV transition of ^{11}B are indicated.

beam direction behind the scattering target in the beginning of each experiment. The measured γ-ray spectrum is corrected for the detector response to extract the shape of the spectral photon beam distribution (black histogram in Fig. 2). Previously known integrated cross sections for transitions from the target itself can be used to determine the absolute photon flux for the associated beam energy settings. For this purpose, at least one level with a known cross section per beam energy is necessary to calibrate the photon flux. From the integrated cross sections for individual excited states in ^{128}Te, that are determined in the NRF measurements using bremsstrahlung at DHIPS, the time-integrated photon flux is computed (red dots in Fig. 2) and used to normalize the photon beam

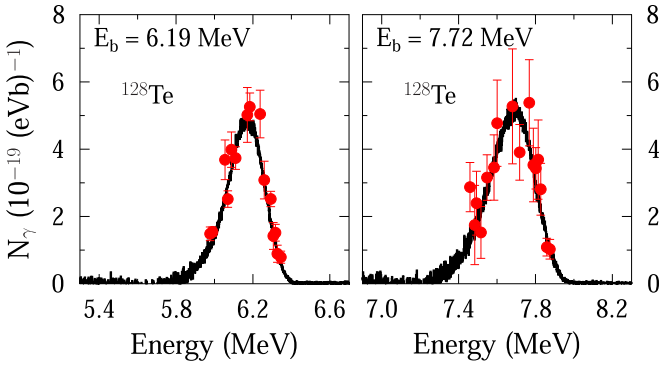

FIG. 2. Spectral beam distributions exemplarily for two beam energies of $E_b = 6.19$ MeV and $E_b = 7.72$ MeV at HIγS (black). The absolute photon flux N_γ is determined by normalization to known integrated cross sections of excited states of ^{128}Te (red dots) determined in the NRF experiment with bremsstrahlung at DHIPS.

distribution. The calibration data points clearly follow the energy distribution of the photon beam.

B. Extraction of photoabsorption cross sections

In addition to a state-by-state analysis quasimonochromatic photon beams enable the extraction of averaged photoabsorption cross sections as a function of the excitation energy. The corresponding method is sketched in Fig. 3. Nuclear levels in a narrow energy window, defined by the width of the quasimonochromatic photon beam of a few hundreds of keV (gray-filled band and gaussian), are excited from the ground state. The intensity of the resonant-absorption process for a given γ-ray energy is governed by the photoabsorption cross section σ_γ, which is difficult to measure directly in real-photon scattering experiments. However, the photoabsorption cross section can be divided into two terms, a so-called "elastic" ($\sigma_{\gamma\gamma}$) and "inelastic" ($\sigma_{\gamma\gamma'}$) part: $\sigma_\gamma = \sigma_{\gamma\gamma} + \sigma_{\gamma\gamma'}$.

1. Elastic cross section

The cumulative intensity measured for transitions of initially excited states directly back to the ground state is related to the "elastic" part displayed as green arrows in Fig. 3(a).

In addition to analyzing isolated transitions, it is possible to extract average cross sections for the energy range covered by the quasimonochromatic photon beam. Figure 4 depicts spectra of ^{128}Te recorded with an HPGe detector (upper panel) and a $LaBr_3$:Ce scintillator (lower panel) with $E_b = 6.4$ MeV. The spectral distribution of the beam is indicated by the dotted line. Both panels show the measured spectrum (black) and the spectrum corrected for the detector response (red) with its 1σ uncertainty band. A detailed description of the deconvolution

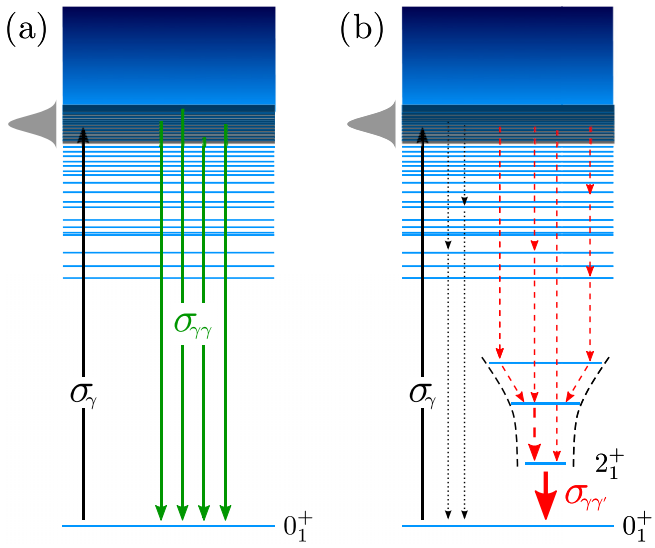

FIG. 3. Illustration of the experimental approach to extract the photoabsorption cross section, $\sigma_\gamma = \sigma_{\gamma\gamma} + \sigma_{\gamma\gamma'}$, from NRF measurements using quasimonochromatic γ-ray beams at HIγS. (a) The "elastic" part $\sigma_{\gamma\gamma}$ is determined by observing all ground-state transitions (green solid arrows). (b) The "inelastic" contribution $\sigma_{\gamma\gamma'}$ is approximated by the ground-state transition intensity of the first (few) 2^+ states (red solid arrow), which are populated by cascading transitions (red dashed arrows). Transitions potentially bypassing the first 2^+ states are indicated (gray dotted arrows).

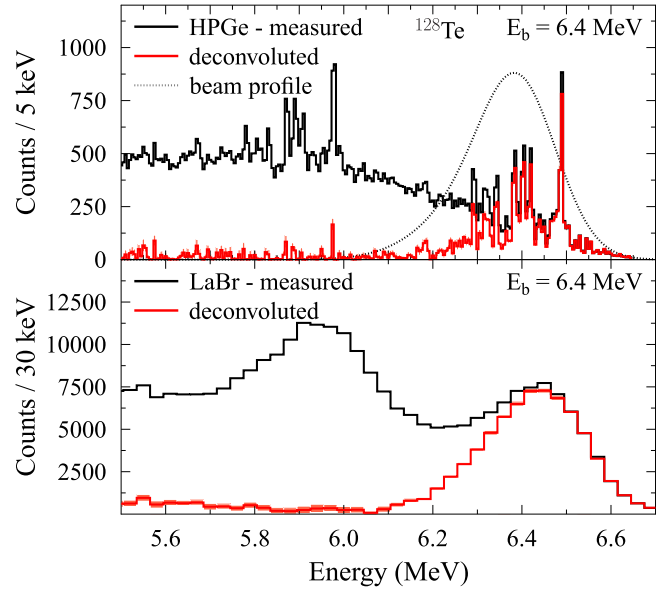

FIG. 4. Typical spectra from single γ-ray spectroscopy (black histograms) recorded with an HPGe (upper panel) and an LaBr (lower panel) detector at a beam energy of $E_b = 6.4$ MeV (dashed line). Deploying a detector-response deconvolution procedure on natural-background corrected γ-ray spectra results in the corresponding red histograms.

procedure can be found in Refs. [47,86]. After the detector response deconvolution only full-energy events are present in the spectra. The upper panel shows, that the observed intensity in the energy region of the beam is located in resolved peaks as well as in the quasicontinuum below those peaks. Due to the inferior energy resolution of the $LaBr_3$:Ce scintillator compared to the HPGe detector, no pronounced structure is observed in the spectrum. However, the photopeak efficiency is about five times higher than for the used HPGe detectors.

The quasicontinuum, sometimes referred to as "unresolved" strength, is the accumulated dipole strength from hundreds to thousands of weakly excited states, while only a few strong dipole transitions are observed as isolated peaks. Since the nuclear level density increases exponentially with the excitation energy, the amount of strength located in the quasicontinuum usually increases compared to the strength in resolved transitions, which will be shown and discussed later based on the available data.

Average cross sections can then be determined accounting for the total strength in a given energy region. The elastic cross section can be expressed with help of Eq. (1) by

$$\sigma_{\gamma\gamma} = \frac{\sum_x I_{0\to x\to 0}}{\Delta E} = \frac{1}{N_T N_\gamma^{\mathrm{tot}}} \sum_x \frac{A_{0\to x\to 0}}{\int_{\Delta\Omega} d\Omega\ \varepsilon(E_x,\Omega) W_{0\to x\to 0}(\Omega)}, \quad (3)$$

with $N_\gamma^{\mathrm{tot}} = \int_0^\infty N_\gamma(E)\,dE$ being the energy-integrated total photon flux. Here, the sum runs over all excited states x in a given energy range ΔE. Thus the full intensity within the excitation energy range defined by the γ-ray beam is integrated whether it is located in the quasicontinuum or in resolved peaks.

2. Inelastic cross section

In analogy to Eq. (3), the inelastic cross section can be defined as

$$\sigma_{\gamma\gamma'} = \frac{\sum_x \sum_{i\neq 0} I_{0\to x\to i}}{\Delta E} = \frac{1}{N_T N_\gamma^{\mathrm{tot}}} \times \sum_x \sum_{i\neq 0} \frac{A_{0\to x\to i}}{\int_{\Delta\Omega} d\Omega\ \varepsilon(E_x - E_i,\Omega) W_{0\to x\to i}(\Omega)}. \quad (4)$$

However, transitions to intermediate levels indicated as red dashed arrows in Fig. 3(b) are usually too weak to be observed directly in single γ-ray spectroscopy measurements. Nevertheless, it is generally assumed that most of the cascading transitions decay via the first low-lying excited 2^+ states [23,39,57,89], which collect the majority of these events. This assumption is backed up by statistical model calculations showing that more than 90% of the cascading events decay via the first few excited 2^+ states depending on the initial excitation energy. Cascades potentially bypassing the low-lying states are shown as gray dotted arrows in Fig. 3(b).

Figure 5 shows the low-energy part of a typical spectrum of ^{128}Te obtained in a measurement with a beam energy of $E_b = 8.56$ MeV. Transitions of the $2^+_{1,2}$ states and the 4^+_1 state are observed including background contamination from ^{228}Ac. These states are not directly excited by the impinging

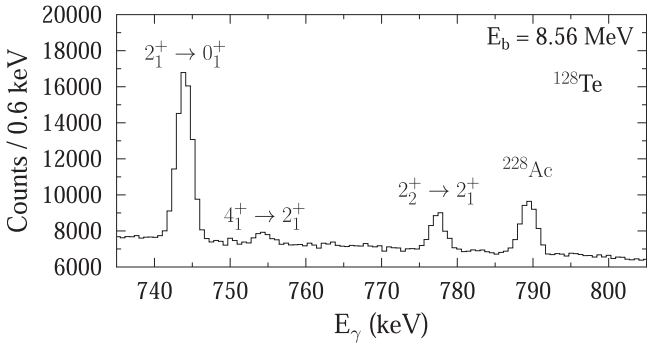

FIG. 5. Typical low-energy part of the γ-ray spectrum recorded with an HPGe detector after photoexcitation of levels of ^{128}Te with $E_b = 8.56$ MeV at HIγS. Decays of the first excited states of ^{128}Te are observed, which are populated via cascade transitions of states excited in the energy region of 8.56 MeV.

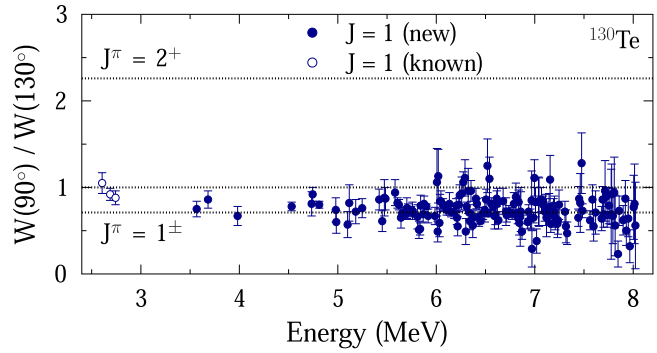

FIG. 6. Angular distribution ratio for the determination of spin-quantum numbers of excited states in ^{130}Te. In total 156 $J^\pi = 1^\pm$ states were observed for the first time (filled blue circles), while three $J^\pi = 1^\pm$ levels were already known before (open blue circles) [80].

photon beam due to its monochromaticity, but are populated by γ cascades. The measured ground-state decay intensity of these states [illustrated as red solid arrow in Fig. 3(b)] present a reasonable approximation of the inelastic cross section and results in the following expression:

$$\sigma_{\gamma\gamma'} \approx \frac{1}{N_T N_\gamma^{\text{tot}}} \sum_j \frac{A_{2_j^+ \to 0_1^+}}{\int_{\Delta\Omega} d\Omega\ \varepsilon(E_{2_j^+}, \Omega)\, W_{2_j^+ \to 0_1^+}(\Omega)}, \quad (5)$$

where the sum runs over the observed ground-state transition of the jth 2^+ state. The angular distribution $W_{2_j^+ \to 0_1^+}(\Omega)$ is determined from the observed asymmetry $\epsilon_{2_1^+}$ of the photons emitted in the decay of the 2_1^+ state. The 2^+ levels can be populated directly by photoexcited states or by cascades via intermediate levels. The latter case results in an approximately isotropic angular distribution, while the decay after the direct feeding of the 2_1^+ shows some degree of anisotropy. For each measurement $W_{2_j^+ \to 0_1^+}(\Omega)$ is computed from the measured asymmetry $\epsilon_{2_1^+}$ assuming a superposition of pure feeding of the 2_1^+ by direct transitions and its population via multiple cascades.

C. Determination of spin-parity quantum numbers

Measurements of angular distributions of emitted γ rays from NRF reactions allow the determination of spin and parity-quantum numbers. As outlined previously, NRF experiments were performed with different photon sources, i.e., with continuous-energy bremsstrahlung and linearly polarized quasimonochromatic photon beams, respectively.

In the following, the two tellurium isotopes will be discussed separately, since the experimental setups differ.

1. ^{130}Te

In NRF measurements mainly dipole and with a smaller probability electric quadrupole transitions are induced. Therefore, only the spin sequences for the excitation of an even-even nucleus from and the subsequent decay back to the ground state are considered, i.e., $0^+ \to 1^\pi \to 0^+$ and $0^+ \to 2^+ \to 0^+$, where $\pi = \pm 1$ is the parity-quantum number of the excited state.

In the DHIPS measurements with ^{130}Te two HPGe detectors were placed at $\vartheta = 90°$ and $\vartheta = 130°$, respectively. Measuring the angular distribution $W(\vartheta)$ of the emitted γ-rays spins of nuclear levels are determined [71]. For dipole and quadrupole excited states the intensity ratios in both HPGe detectors are expected to be $W_{0\to1\to0}(90°)/W_{0\to1\to0}(130°) = 0.71$ and $W_{0\to2\to0}(90°)/W_{0\to2\to0}(130°) = 2.26$, respectively. For isotropically distributed γ-rays the ratio is equal to unity. Due to the substantial difference between the two ratios, spin-quantum numbers can be assigned to even weakly excited states. The experimental data for ^{130}Te above 2.5 MeV are shown in Fig. 6. All observed transitions are assigned to be ground-state transitions from $J^\pi = 1^\pm$ states of which 156 excited states are observed for the first time (filled blue circles). Three of the observed low-lying $J^\pi = 1^\pm$ states (open blue circles) are known from previous studies [78,79]. Their measured values of $W(90°)/W(130°) \approx 1$ indicate that these levels are not solely excited by the impinging photon beam, but also populated by energetically higher-lying excited states, which changes the angular distribution towards isotropy.

For the determination of the electromagnetic character of the observed dipole strength the NRF data from HIγS are used. Exploiting the linear polarization of the photon beam allows for an unambiguous distinction between $E1$ and $M1$ transitions [90]. The angular distribution for the spin sequence $0^+ \xrightarrow{\vec{\gamma}} 1^\pi \xrightarrow{\gamma'} 0^+$ induced by linearly polarized photon beams in the entrance channel is described by

$$W(\vartheta, \varphi) = \frac{3}{4}\left[1 + \cos^2(\vartheta) + \pi \cos(2\varphi)\, \sin^2(\vartheta)\right]. \quad (6)$$

The parameter π depends on the parity-quantum number of the excited state and is -1 $(+1)$ for negative (positive) parity. The angular distribution in Eq. (6) shows distinct minima and maxima for $E1$ and $M1$ transitions at perpendicular directions with respect to the incoming beam. Hence, it is sufficient to measure the intensity of the scattered photons at $\varphi = 0°$ and $\varphi = 90°$, respectively. The maximum analyzing power Σ is

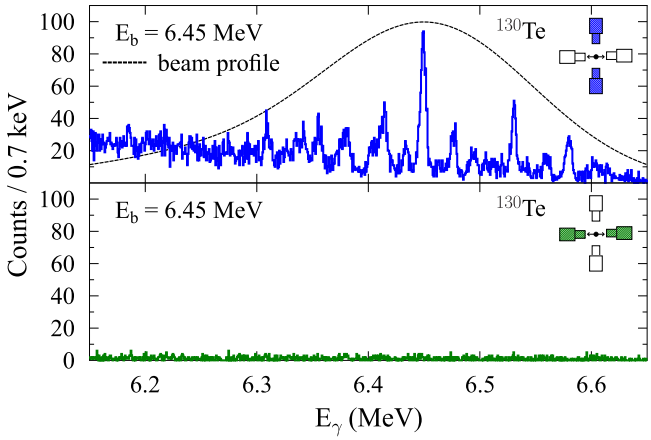

FIG. 7. Obtained γ-ray spectra at a beam energy of $E_b = 6.45$ MeV with HPGe detectors placed perpendicular (upper panel) and parallel (lower panel) to the polarization plane indicated by the double-sided arrow.

realized for $\vartheta = 90°$:

$$\Sigma = \frac{W(90°, 0°) - W(90°, 90°)}{W(90°, 0°) + W(90°, 90°)} = \pi = \begin{cases} +1 & \text{for } J^\pi = 1^+ \\ -1 & \text{for } J^\pi = 1^- \end{cases}. \quad (7)$$

Therefore, a crosslike detector setup consisting of four HPGe detectors was mounted perpendicular with respect to the beam direction. For the experimental determination of parity-quantum numbers the asymmetry ϵ is defined by means of the efficiency-corrected peak areas observed in the γ-ray spectra of the horizontal (N_h) and the vertical (N_v) detectors:

$$\epsilon = \frac{N_h - N_v}{N_h + N_v} \propto \Sigma, \quad (8)$$

which is proportional to the analyzing power.

The measurements were conducted for beam energies between 5.5 and 8.5 MeV in steps of roughly 250 keV. Figure 7 shows typical γ-ray spectra at $E_b = 6.45$ MeV obtained perpendicular (blue) and parallel (green) to the beam polarization plane (indicated by the double-sided arrow). The beam profile is given as a dashed curve. Peaks stemming from ground-state transitions of excited states in ^{130}Te are observed in the vertical detectors, only. This observation shows that this excitation-energy range is dominated by $J^\pi = 1^-$ states.

The experimental results for the asymmetries of individual transitions are shown in the upper panel of Fig. 8. In the covered energy range exclusively $J^\pi = 1^-$ states are observed, confirming that the dipole strength below the neutron separation threshold in ^{130}Te is dominated by $E1$. This observation is further supported by an analysis of the spectra corrected for detector response (similar to Fig. 4 for ^{128}Te). The continuum in the γ-ray spectra including contributions from unresolved transitions is taken into account by integration of the full intensity in the excitation-energy region. The corresponding average asymmetry $\langle\epsilon\rangle$ of the integrated and efficiency-corrected ground-state transition intensities observed in the horizontal and vertical HPGe detectors is displayed in the lower panel of Fig. 8. The dipole strength is dominated by the $E1$ response even if unobserved ground-state transitions are taken into account. However, the fraction of $M1$ strength is not zero in the covered energy region and can be extracted from the data, which will be discussed later in this article.

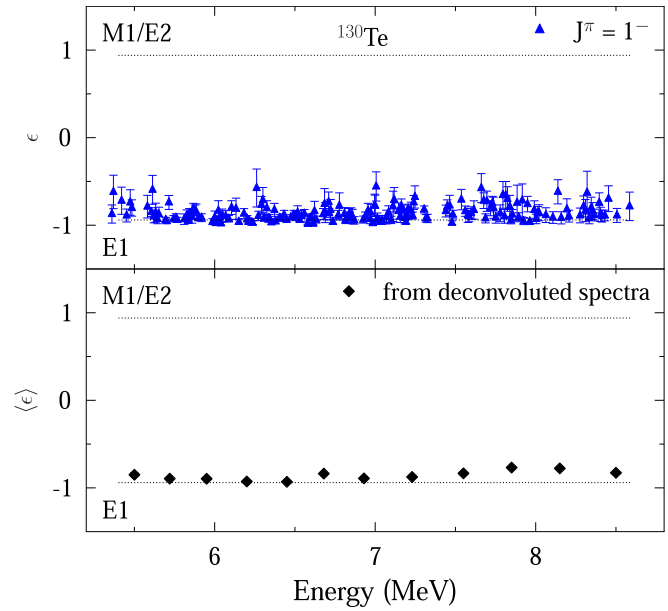

FIG. 8. Experimental asymmetries determined for individual nuclear transitions (upper panel) observed in ^{130}Te and averaged over the excitation-energy range defined by the spectral distribution of the monoenergetic γ-ray beam (lower panel). The dotted horizontal lines indicate the simulated expectation values taking the detector geometry into account for pure $E1$ and $M1$ or $E2$ transitions, which cannot be distinguished in the given setup geometry.

2. ^{128}Te

In the case of ^{128}Te, the spin and parity assignments are deduced simultaneously in the experiments at HIγS due to the specific detector setup geometry. In addition to the horizontal and vertical HPGe detector two detectors are placed at backward angles ($\vartheta = 135°$, $\varphi = 225°$ and 315°). Typical spectra from the HIγS measurements for ^{128}Te are shown in Fig. 9 with a beam energy of $E_b = 4.33$ MeV and its spectral distribution indicated by the dashed curve in Fig. 9(a). Comparing the three spectra, spin and parity quantum numbers can be extracted. The vertical and horizontal detectors are sensitive to the parity of excited states, while the backward-placed detector allows for a distinction between 1^+ and 2^+ states. All observed transitions are indicated by vertical dotted lines. Similar to the analysis of the ^{130}Te data, the experimental asymmetries for individual excited states and averaged over a given excitation-energy region are shown in the upper and lower panel of Fig. 10, respectively. While most of the observed ground-state transitions are assigned to origin from 1^- states (blue triangles), twelve levels below 4.5 MeV exhibit positive parity-quantum numbers (green circles, orange asterisks, and black squares). The average asymmetries $\langle\epsilon\rangle$ are shown in the lower panel of Fig. 10. Above 5 MeV excitation

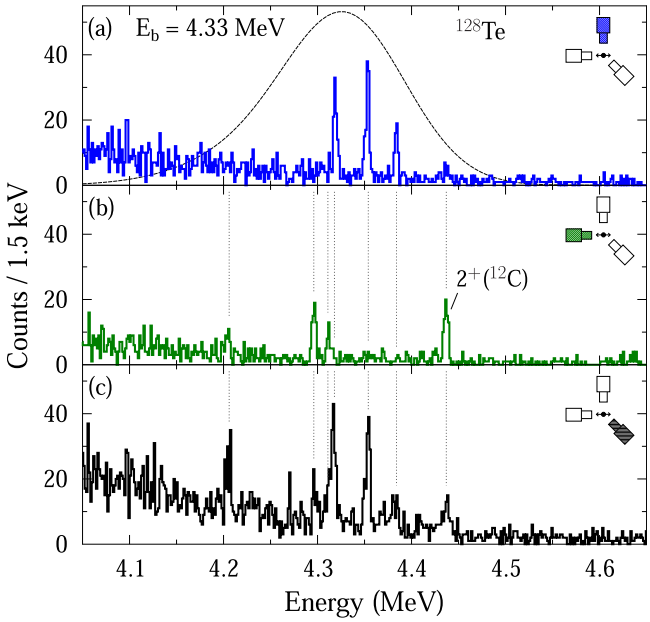

FIG. 9. Experimental γ-ray spectra obtained for ^{128}Te with HPGe detectors placed perpendicular (a) and parallel (b) to the beam's polarization plane. Panel (c) shows the γ-ray spectrum recorded at a backward position defined in Table II. The spectral distribution of the incoming γ-ray beam with $E_b = 4.33$ MeV (dashed line) is displayed in (a). The dashed vertical lines indicate all observed transitions in this measurement.

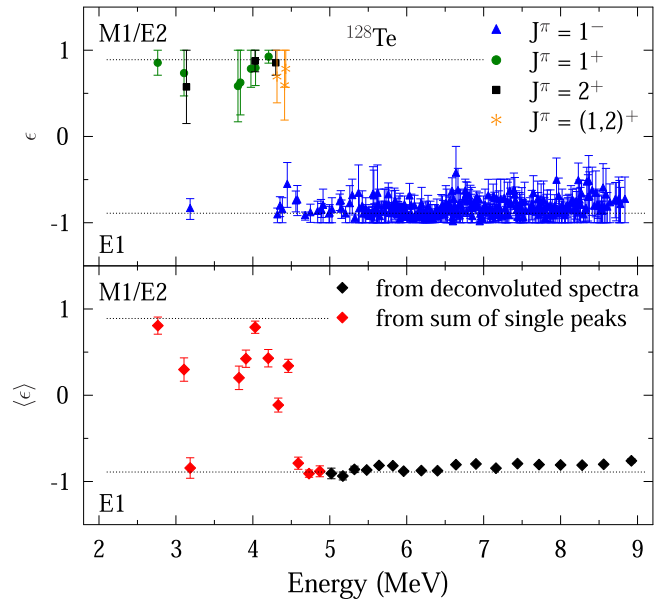

FIG. 10. Experimental asymmetries determined for individual nuclear transitions (upper panel) observed in ^{128}Te and averaged over the excitation-energy range defined by the spectral distribution of the monoenergetic γ-ray beam (lower panel). The dotted horizontal lines indicate the expectation values for pure $E1$ and $M1$ or $E2$ transitions, which cannot be distinguished in the given setup geometry.

energy the $\langle\epsilon\rangle$ values (black diamonds) are extracted from γ-ray spectra that are corrected for detector response and include unresolved transitions in the same fashion as for ^{130}Te. At lower energies, contributions from unresolved transitions are not present. For each beam-energy setting only a few individual transitions are observed, which are used to compute an average asymmetry (red diamonds).

It is crucial to take the backward-placed detectors into account for the separation of $M1$ and $E2$ transitions. Using the angular distribution for a $0^+ \xrightarrow{\vec{\gamma}} 2^+ \xrightarrow{\gamma'} 0^+$ cascade,

$$W(\vartheta,\varphi) = \frac{5}{8}\{2+\cos(2\vartheta)+\cos(4\vartheta) - [2+4\cos(2\vartheta)]\cos(2\varphi)\sin^2(\vartheta)\}, \quad (9)$$

in combination with Eq. (6), two asymmetries ϵ_v and ϵ_h are defined to assign spin-parity quantum numbers J^π to individual excited states:

$$\epsilon_v = \frac{N_v - N_b}{N_v + N_b}, \quad (10)$$

$$\epsilon_h = \frac{N_h - N_b}{N_h + N_b}, \quad (11)$$

with N_v, N_h, and N_b being the efficiency-corrected peak areas observed in the γ-ray spectra of the vertical, horizontal, and backward detectors.

Figures 11(a) and 11(b) display the experimental results for all ground-state transitions of excited states of ^{128}Te between 2.5 and 9.5 MeV. The dashed lines indicate the expectation values for 1^- (blue), 1^+ (green), and 2^+ (black) states, respectively. The comparison of the statistical uncertainties for a particular transition in both asymmetry plots shows that ϵ_v is more sensitive to 1^- states, while ϵ_h exhibits an increased sensitivity for the separation of 1^+ and 2^+ states. Thus, even in cases with low counting statistics, the combination of ϵ_v and ϵ_h allows for an unambiguous determination of J^π in a single experiment. A particular spin-parity quantum number is assigned to a given nuclear level, if its experimental asymmetries are in agreement with the corresponding expectation values for both ϵ_v and ϵ_h within two standard deviations. If this condition applies to more than one spin-parity value, both possible quantum numbers are given.

The information of both quantities, ϵ_v and ϵ_h, are combined in the correlation shown in Fig. 11(c). A clear separation between 1^- states and $(1,2)^+$ states is observed and illustrates the sensitivity for the distinction between 1^- states, on the one hand, and 1^+ and 2^+ states, on the other hand. For instance, the nuclear level at 3136 keV [black square with $\epsilon_v = 0.44(55)$ in Fig. 11(a)] indicates $J^\pi = 1^-$ although a $J^\pi = 2^+$ assignment is also possible within a 2σ interval. Taking the additional information of $\epsilon_h = 0.70(32)$ into account, this state is assigned to be a 2^+ state since $J^\pi = 1^-$ can be excluded by more than 4σ, which is in agreement with the findings in Ref. [76]. The energy region above 4 MeV is dominated by 293 excited states with $J^\pi = 1^-$ (blue triangles). Between 2.7 MeV and 5.5 MeV six states are assigned $J^\pi = 1^+$ (green circles), three states have $J^\pi = 2^+$ (black squares), and for three levels only positive parity can be assigned, hence labeled with $J^\pi = (1,2)^+$ (orange asterisks).

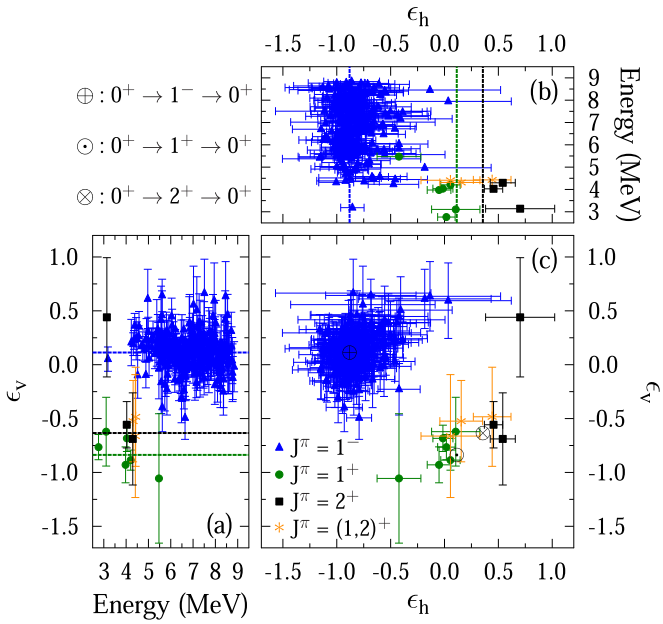

FIG. 11. Experimental asymmetries ϵ_v (a) and ϵ_h (b) obtained with the γ^3 setup for ^{128}Te in the excitation-energy range from 2.7 to 9.0 MeV. The correlation of both asymmetries (c) enables a simultaneous assignment of spin and parity-quantum numbers.

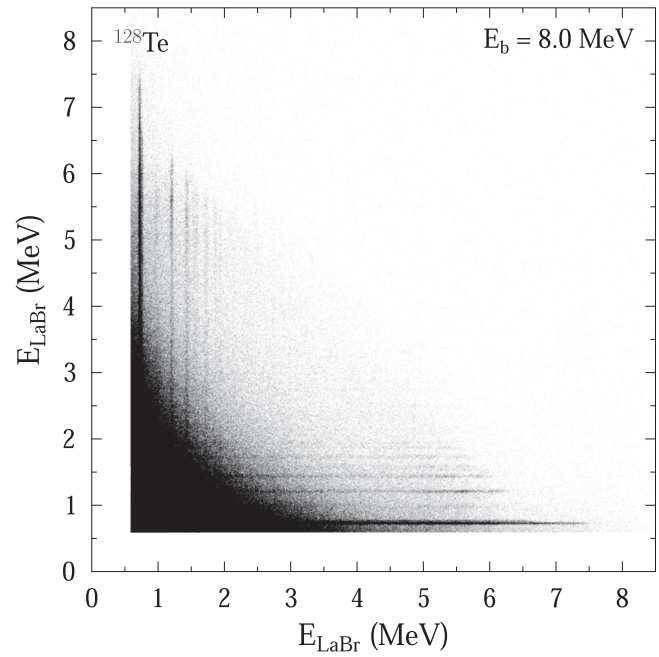

FIG. 12. Summed matrix for all combinations of γ-γ coincidences between two LaBr detectors at $E_b = 8.0$ MeV. Low-energy trigger thresholds are set to ≈600 keV to reduce the dead time of the detection system.

D. γ-γ coincidence measurements with ^{128}Te

So far, the analysis concentrated on data obtained from single γ-ray spectroscopy measurements. For the investigation of the dipole response of ^{128}Te, the γ^3 setup is used for γ-γ coincidence experiments to study the γ decay branching ratios of photo-excited states as a function of the excitation energy. Due to the superior full-energy γ-ray efficiency of the LaBr scintillators compared to the HPGe detectors, the following section focuses on the analysis of γ-γ correlations between LaBr detectors.

The summed symmetric LaBr-LaBr coincidence matrix from the measurement with $E_b = 8.0$ MeV is shown in Fig. 12 with a low-energy threshold of ≈600 keV. Since the energy of the incident photon beam is quasimonochromatic, the summed energy measured in two detectors is limited to E_b resulting in a triangular shape apparent in the coincidence matrix. Several prominent lines are observed that highlight coincident events with the corresponding γ-ray energy.

The projection of the LaBr-LaBr matrix to one of the axes is shown for the energy region from 0.6 to 1.6 MeV in the insets of Figs. 13(a) and 13(c). Transitions from low-lying excited states, in particular 2^+ states are observed. The blue and green hatched regions mark the $2_1^+ \to 0_1^+$ and $2_3^+ \to 2_1^+$ transitions, respectively, while the gray cross-hatched areas indicate regions associated to random-coincidence background. In the measurements with $E_b \geqslant 6.4$ MeV primary transitions to low-lying excited states up to 2.7 MeV level energy are observed taking the summed statistics of all LaBr detectors into account.

Figure 13 shows a comparison of the coincidence spectra extracted from setting cuts on low-energy γ-rays corresponding to specific transitions between low-lying excited states. The energy cut on the ground-state transition of the 2_1^+ state (blue-hatched region) generates a coincident γ-ray spectrum [blue histogram in Fig. 13(a)] with maximum γ-ray energies at around E_b-$E_{2_1^+}$. This spectrum contains all events that were observed in coincidence to the decay of the 2_1^+ as well as random coincidences with background radiation in this energy region. The contribution of the background originating from random coincidences [gray histogram in Fig. 13(a)] is determined from energy cuts right above the energy of the $2_1^+ \to 0_1^+$ transition (gray cross-hatched area) and the gated spectrum (blue) is corrected for these events. The same procedure is applied to the analysis of primary γ-ray transitions to further low-lying levels such as the $2_3^+ \to 2_1^+$ transition [green histogram and green-hatched area in Fig. 13(c)]. Due to the relative energy resolution of about 3 % at 1 MeV for the LaBr detectors, it is not possible to set separate energy cuts on the decays of the 2_3^+ and 0_2^+ state, therefore their population is jointly analyzed. The events located at the high-energy end of the spectra correspond to direct transitions from excited states at E_b to the associated lower-lying excited states. To extract merely full-energy events, a detector response deconvolution has to be performed in analogy to the example shown in Fig. 4. The resulting spectrum from the energy cut on the $2_1^+ \to 0_1^+$ transition is displayed in Fig. 13(b). An accumulation of events with a distribution similar to the incoming γ-ray beam (dotted curve) is observed at $E_b - E_{2_1^+} = 7.25$ MeV. The limited energy resolution of the LaBr detectors inhibits the observation of isolated transitions. However, the total intensity observed at $E_b - E_{2_1^+}$ is directly proportional to the average branching ratio to the 2_1^+ state including also weak transitions. The events below 7 MeV result from transitions to further

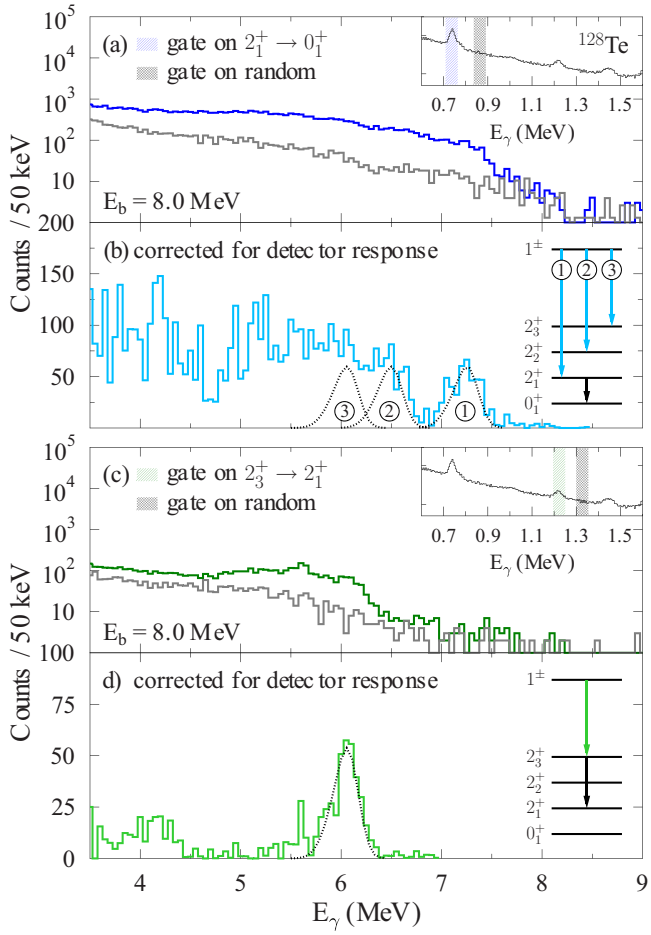

FIG. 13. Gated spectra of the γ-γ coincidence matrix shown in Fig. 12. Insets: Low-energy region of the projection from LaBr-LaBr coincidences below 1.6 MeV. The hatched and cross-hatched areas correspond to applied gates on γ-ray transitions of ^{128}Te and on random background radiation, respectively. For details see text.

low-lying excited states such as the 2_2^+ and 2_3^+ states indicated by the dotted curves at 6.5 and 6 MeV, respectively, that are observed in coincidence to the $2_1^+ \rightarrow 0_1^+$ transition. It is emphasized, that due to the overlap of contributions from several primary transitions to different low-lying levels, it is not trivial to extract the individual intensities from the spectrum in Fig. 13(b). Indeed, the sensitivity is substantially increased by gating on appropriate transitions to extract primary transitions to distinct low-lying levels. A typical example is given in Fig. 13(d) selecting all events that are coincident to the $2_3^+ \rightarrow 2_1^+$ transition, subtracting random background, and applying a detector-response correction of the γ-ray spectrum. A clean signal is identified at around 6 MeV, which is assigned to direct transitions from excited levels at E_b to the 2_3^+ state. The measured full intensities for all observed primary γ-ray transition channels populating low-lying levels such as the 2_1^+ up to the 2_8^+ state are converted into cross sections and branching ratios, which will be discussed in the course of the following section.

IV. RESULTS AND DISCUSSION

The following section is divided into two parts. At first the results for both tellurium isotopes from a state-by-state analysis will be compared and discussed in connection with theoretical calculations within the QPM [74]. The second part is dedicated to the discussion of average quantities, such as photoabsorption cross sections and average branching ratios.

A. State-by-state analysis

In the following the focus is on the discussion of the $E1$ strength distribution measured for ^{128}Te and ^{130}Te. The reduced $E1$ transition probability

$$\frac{B(E1)\uparrow}{\mathrm{e^2fm^2}} = 2.486 \times 10^{-4} \frac{\Gamma}{\Gamma_0} \frac{I_{0\rightarrow x\rightarrow 0}}{\mathrm{eV\,b}} \frac{\mathrm{MeV}}{E_x} \qquad (12)$$

can be directly computed from the measured integrated scattering cross section $I_{0\rightarrow x\rightarrow 0}$ (given in units of eV b) of the ground-state decay channel and the initial excitation energy E_x (in MeV). The determined $B(E1)\uparrow$ values for ^{128}Te and ^{130}Te are shown in Figs. 14(a) and 14(b), respectively, assuming $\Gamma_0/\Gamma = 1$ for all states where no transitions to low-lying levels other than the ground state were observed. In principle, many unobserved weak branching transitions could add up and contribute to the total transition width Γ resulting in a too low Γ_0/Γ. However, in experiments using the self-absorption technique on ^{140}Ce [91] no significant deviation from $\Gamma_0/\Gamma = 1$ was observed for the strongly excited states analyzed. In both tellurium isotopes, a concentration of E1 strength is apparent around 6.5–7.0 MeV. The summed strength for isolated transitions between 5 and 8 MeV in ^{128}Te is found to be $\sum B(E1)\uparrow = 0.367(48)$ e^2 fm^2, while the total strength in the same energy range for ^{130}Te is about 30% larger being $\sum B(E1)\uparrow = 0.473(36)$ e^2 fm^2.

The experimental results are compared to calculations within the quasiparticle phonon model (QPM) [74]. In this model, excited states in even-even nuclei are treated in terms of phonons. For the current calculations, the $1p1h$ doorway 1^- states are coupled to complex $2p2h$ and $3p3h$ configurations. The obtained fragmentation is in good agreement with the experimentally observed strength distribution for isolated transitions and was studied in several nuclei before [46,92]. The calculated $B(E1)\uparrow$ values for ^{128}Te and ^{130}Te are shown in Figs. 14(c) and 14(d). A similar accumulation of $E1$ strength below the neutron separation thresholds is evident in the QPM calculations describing sufficiently well the individual transition strengths on an absolute scale. The calculated strength summed up between 5 and 8 MeV are $\sum B(E1)\uparrow = 0.569$ e^2 fm^2 and $\sum B(E1)\uparrow = 0.529$ e^2 fm^2 for ^{128}Te and ^{130}Te, respectively. The difference between the calculated total strength and the measured cumulated strength in isolated states may be explained by two aspects. Firstly, the ground-state branching ratio Γ_0/Γ is experimentally unknown for most of the excited states, which would lead to increased $B(E1)\uparrow$ values, if $\Gamma_0/\Gamma < 1$. The second reason is the experimental sensitivity limit in the NRF measurements, which is determined following the formalism given in Ref. [93] and indicated for the DHIPS experiments using bremsstrahlung in

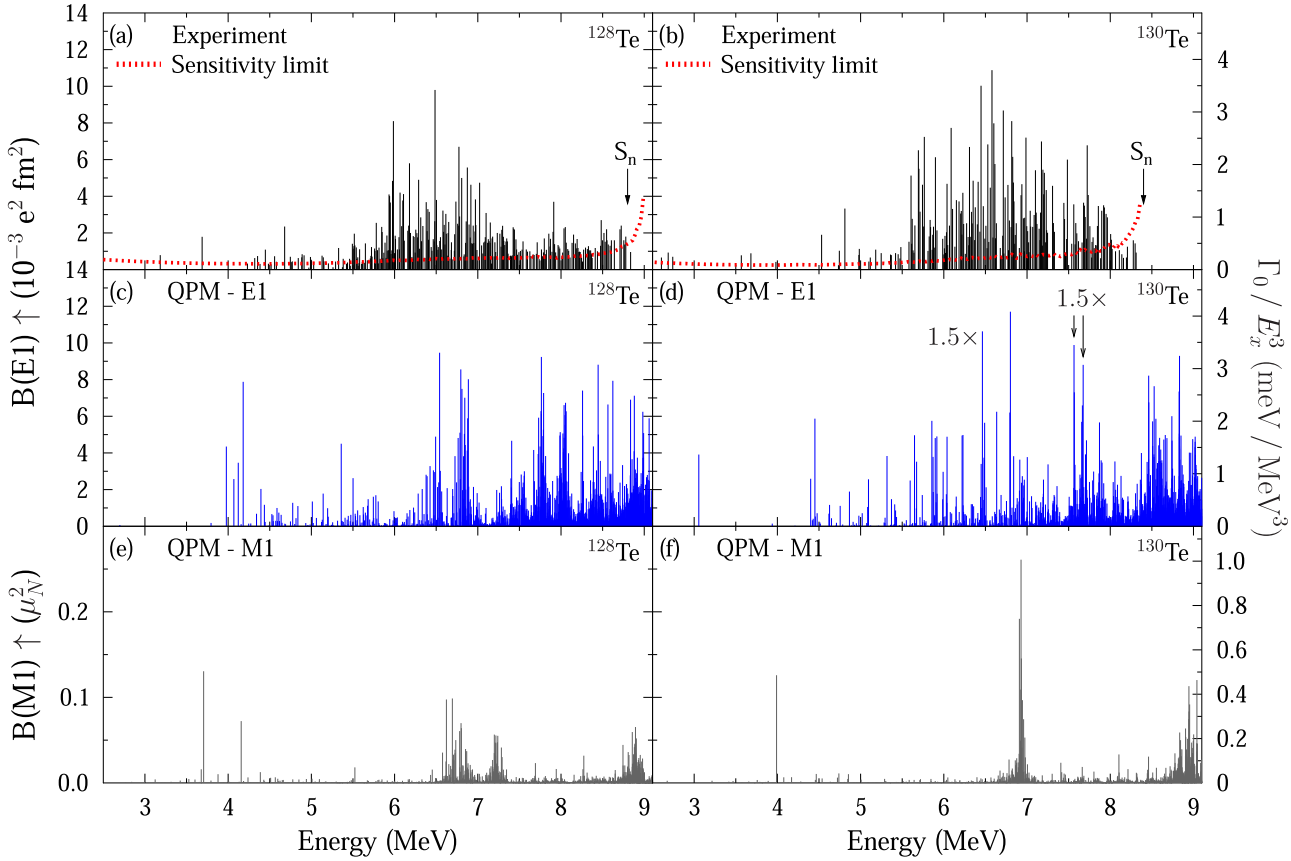

FIG. 14. Experimental $E1$ strength distribution for ^{128}Te (a) and ^{130}Te (b) with the corresponding experimental sensitivity limit displayed as red-dotted line. Values from QPM calculations are shown in (c) for ^{128}Te and in (d) for ^{130}Te, where the marked values are scaled down by a factor of 1.5 for a better display. Predicted $M1$ excitations are shown for both nuclei in panels (e) and (f). See text for details.

Figs. 14(a) and 14(b) by the red-dotted lines. All excited states that have ground-state transition strengths close to or smaller than the sensitivity limit are not observed in a state-by-state analysis at DHIPS. The sensitivity is slightly increased by the use of the monoenergetic γ-ray beams at HIγS, which made it possible to observe additional weakly excited states that are included in Figs. 14(a) and 14(b).

The predicted $M1$ strength is shown in Figs. 14(e) and 14(f) for ^{128}Te and ^{130}Te, respectively. The dominant part of the computed $M1$ strength in both tellurium isotopes is carried by the $\pi\, 1g_{9/2} \rightarrow 1g_{7/2}$ and $\nu\, 1h_{11/2} \rightarrow 1h_{9/2}$ spin-flip excitations at about 7 MeV for the proton contribution and at around 9 MeV for the neutron part. However, in the NRF measurements no resolved $M1$ transitions were observed at those excitation energies. The corresponding reduced transition widths Γ_0/E_i^3 are indicated on the right-hand side ordinate in Fig. 14. Note the difference in scale between $E1$ and $M1$ transitions. The $M1$ excitations are about one order of magnitude weaker than the $E1$ transitions and, thus are expected to be below the experimental sensitivity limits of the NRF experiments. Interestingly, in the QPM calculations for ^{128}Te, two relatively strong $M1$ fragments are located at 4 MeV originating from the neutron $\nu\, 2d_{5/2} \rightarrow 2d_{3/2}$ spin-flip excitation. Taking the summed strength of all $M1$ excitations between 3.7 and 4.2 MeV results in $B(M1)\uparrow_{\mathrm{QPM}} = 0.225\ \mu_N^2$. They most likely correspond to the four experimentally identified $M1$ transitions at similar excitation energies of 3809.5, 3975.9, 4035.6, and 4204.0 keV having a total strength of $B(M1)\uparrow_{\mathrm{exp}} = 0.323(32)\ \mu_N^2$.

As the nuclear level density increases with the excitation energy, more and more $E1$ strength remains unobserved in the experiment, while the QPM calculations include all possible excitations independent of their individual strength. This aspect was part of studies comparing the fragmentation in NRF experiments to theoretical calculations (see Refs. [46,92]). This downside of classical NRF experiments with bremsstrahlung is resolved by analyzing the full γ-ray spectrum including unobserved transitions using quasi-monochromatic photon beams and will be discussed in the subsequent section.

B. Average quantities

In the data analysis section of this article, a method was outlined to extract averaged photoabsorption cross sections from NRF measurements at HIγS. Using Eq. (3), the elastic cross section is extracted at all beam-energy settings for both

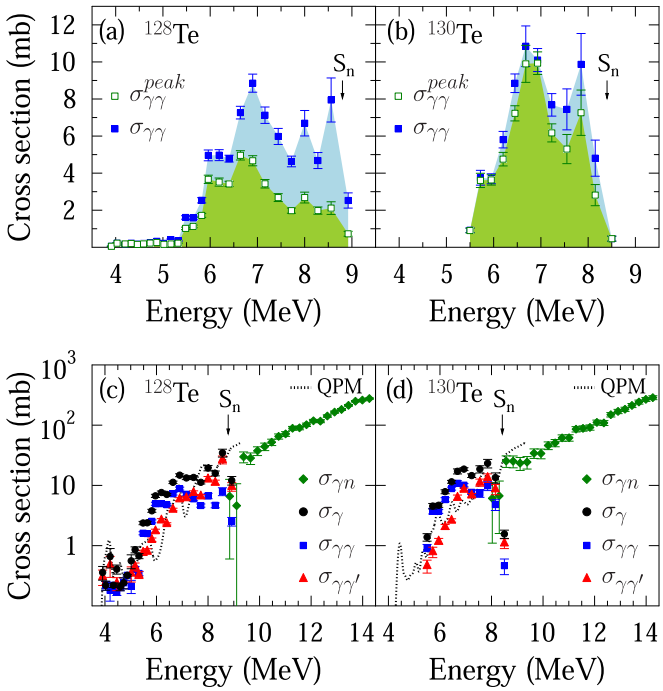

FIG. 15. Average cross sections for ^{128}Te and ^{130}Te. Elastic cross sections are determined accounting for isolated transitions (open green squares) and including contributions from unresolved transitions (blue squares) shown in panels (a) and (b). A comparison of the total photoabsorption cross sections (black dots), the complete elastic cross sections (blue squares), and the inelastic cross sections (red triangles) to (γ, n) cross sections (green diamonds) from Ref. [94] and computed values in the QPM (dotted line) is displayed in panels (c) and (d). For a detailed discussion see text.

tellurium isotopes. Figure 15(a) shows two types of elastic cross sections determined for ^{128}Te. One is determined from the sum of isolated peaks in the HPGe spectra ($\sigma_{\gamma\gamma}^{\text{peak}}$, open green squares). The second one takes into account the complete spectrum after deconvolution of the detector response, i.e., considering resolved and unresolved transitions ($\sigma_{\gamma\gamma}$, blue squares). In ^{128}Te, the dipole strength below 5 MeV is mainly apparent in isolated peaks in the HPGe γ-ray spectra, while at higher energies the unresolved strength from weakly excited states located in the quasicontinuum cannot be neglected. In fact, the unresolved strength accounts for about 20% of the total elastic cross section at 5.5 MeV increasing monotonously up to 70% at 8.9 MeV.

The same analysis is performed for ^{130}Te between 5.5 and 8.5 MeV. Figure 15(b) compares the elastic cross sections measured for individual transitions to the one extracted from the full spectra. A few percent of the complete ground-state transition strength is missed at 5.5 MeV, if only resolved transitions are analyzed, while roughly 40% is located in the quasicontinuum at 8.2 MeV. This is in accordance to the calculated strength distributions in Figs. 14(c) and 14(d), where more $E1$ strength is distributed to many weakly excited states in ^{128}Te than in ^{130}Te. This is due to the increased collectivity of the 2_1^+ and 3_1^- phonons in ^{128}Te as compared to ^{130}Te, where an enhanced coupling of the doorway 1^- states with complex two-phonon configurations leads to stronger fragmentation of the doorway configurations strength.

The elastic (blue squares), inelastic (red triangles), and the total photoabsorption cross sections (black dots) deduced with the method discussed in the context of Fig. 3 are shown in Figs. 15(c) and 15(d) for ^{128}Te and ^{130}Te, respectively. In both isotopes, $\sigma_{\gamma\gamma'}$ is steadily increasing with the excitation energy, while $\sigma_{\gamma\gamma}$ saturates and decreases above 6.5 MeV. In ^{128}Te, above 7 MeV σ_γ is clearly dominated by the inelastic contribution, in contrast to ^{130}Te where this effect is observed to be weaker. Under the assumption that $E1$ excitations dominate, the observed strength in the range from 5.5 and 8.5 MeV exhausts about 2.3(1)% and 1.8(2)% of the Thomas-Reiche-Kuhn sum rule [95,96] in ^{128}Te and ^{130}Te, respectively, which is consistent with nuclei in the same mass region [8]. A smooth continuation from the photoabsorption cross sections below the neutron binding energies S_n toward (γ, n) cross sections $\sigma_{\gamma n}$ (green diamonds) [94] is observed for both isotopes.

The photoabsorption cross sections determined from the QPM are depicted as dotted lines. A moving average is computed from the individual excitations weighted by a Gaussian with a FWHM of about 3% of its mean value. The QPM calculations were performed up to an cutoff energy of 9.5 MeV, which is above the neutron separation thresholds of both tellurium isotopes. Therefore, the measured photoabsorption cross sections rapidly decline at the corresponding neutron separation energies, while the calculations continue to increase with higher excitation energies towards the IVGDR. The QPM cross sections are in good agreement with the experimental findings. In particular, the order of magnitude is well described and bumplike structures are observed in the QPM calculations below 8.5 MeV.

Recently, the photoabsorption cross sections in ^{120}Sn extracted from (p, p') experiments [51] were compared to data from (γ, γ') measurements, that accounted for resolved ground-state transitions, only. With increasing excitation energy the results from (p, p') diverge from the NRF data by almost a factor of ten close to the neutron threshold. Obviously, the deviation is due to unobserved strength from contributions of the quasicontinuum and inelastic decay channels in the NRF measurements. A very recent high-sensitivity study resolved most of the discrepancy by accounting for the quasicontinuum and correcting for average decay branching ratios calculated in the extreme statistical model [52]. However, the photoabsorption cross sections from the continuum analysis exceed the (p, p') data on average by about 50% between 5.9 and 8.7 MeV. In the isotopes ^{128,130}Te, an increasing ratio is observed between σ_γ and $\sigma_{\gamma\gamma}^{\text{peak}}$ of up to 16 at 8.5 MeV for ^{128}Te and a factor of 5 at 8.3 MeV for ^{130}Te, which is in the range of the discrepancy discussed in [51]. Thus, it follows that it is necessary to consider the quasicontinuum and inelastic decay channels in NRF experiments to make a reasonable comparison to complementary reactions such as inelastic proton scattering.

The study of average quantities shown in the present work highlights the importance and the potential of photon-scattering experiments with quasimonochromatic γ-ray beams as a complementary and model-independent

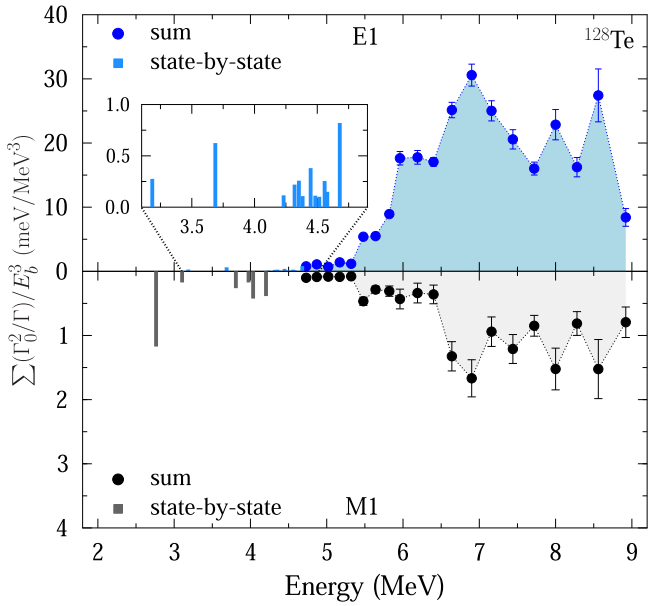

FIG. 16. Separation of the elastic cross sections into contributions from $E1$ and $M1$ transitions for ^{128}Te. Above 4.5 MeV a decomposition of the complete elastic cross sections presented in Fig. 15(a) is performed for each beam-energy setting. The summed reduced ground-state transition widths are displayed for the $E1$ (blue circles) and the $M1$ parts (black circles). Below 4.5 MeV in light blue and light gray bars the results for individual transitions are shown.

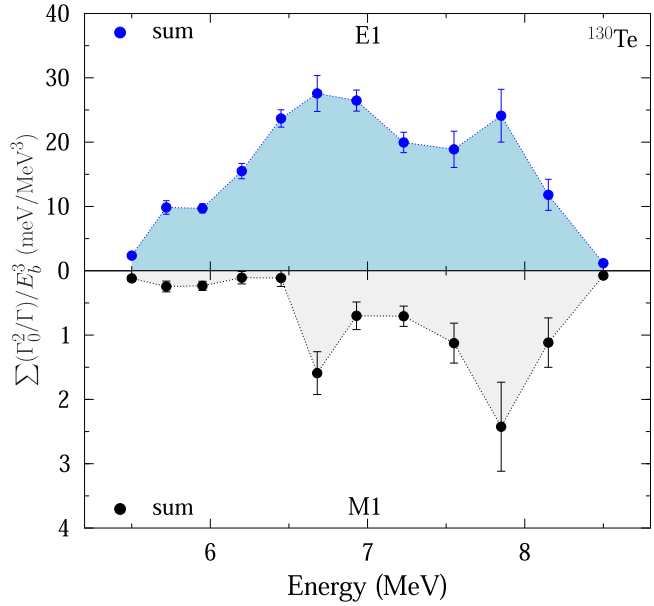

FIG. 17. Separation of the elastic cross sections into contributions from $E1$ and $M1$ transitions for ^{130}Te. A decomposition of the complete elastic cross sections shown in Fig. 15(b) is performed for each beam-energy setting. The summed reduced ground-state transition widths are displayed for the $E1$ (blue circles) and the $M1$ parts (black circles).

approach for the extraction of complete photoabsorption cross sections.

C. Average $E1$ and $M1$ ground-state transition strength

The measured asymmetries for ^{130}Te and ^{128}Te displayed in Figs. 8 and 10 show qualitatively that the dipole response in this energy regime is dominated by $E1$ excitations. Although, no distinct resolved $M1$ transitions are observed above 5 MeV, the contribution from unresolved $M1$ strength is nonzero. A separation of the elastic cross section into $E1$ and $M1$ contributions is achieved by a decomposition of the γ-ray spectra. The measured ground-state transition intensity in one LaBr detector is proportional to the sum of $E1$ and $M1$ contributions,

$$N \propto I_{E1}\,\langle \varepsilon W \rangle^{E1} + I_{M1}\,\langle \varepsilon W \rangle^{M1}\,, \tag{13}$$

where I_{E1} and I_{M1} are the summed energy-integrated cross sections for $E1$ and $M1$ ground-state transitions in a given excitation-energy window, respectively. The quantities $\langle \varepsilon W \rangle^{E1}$ and $\langle \varepsilon W \rangle^{M1}$ represent the average efficiency-weighted angular distributions for $0^+ \to 1^- \to 0^+$ and $0^+ \to 1^+ \to 0^+$ transitions, respectively.

The results for both tellurium isotopes are presented in Figs. 16 and 17. Note the difference in scale by a factor of ten between the upper and lower panels showing the extracted reduced $E1$ and $M1$ strength. The dipole response above 5 MeV is clearly dominated by $E1$ excitations, which is consistent with QPM calculations comparing the expected total $E1$ and $M1$ strength in this energy region (see Fig. 14). The calculated $M1$ strength from 6.5 to 7.5 MeV ($\pi\, 1g_{9/2} \to 1g_{7/2}$ spin-flip) is about 3 μ_N^2 and 2.4 μ_N^2 for ^{128}Te and ^{130}Te, respectively. The summed strength from 8.5 to 9.5 MeV ($\nu\, 1h_{11/2} \to 1h_{9/2}$ spin-flip) accounts to roughly 6 μ_N^2 (10 μ_N^2) in ^{128}Te (^{130}Te). The experimentally determined energy region of the $M1$ transitions to the ground state is in fair agreement with the QPM calculations shown in Figs. 14(e) and 14(f). The experimental summed $M1$ strength between 6.5 and 8.5 MeV is 2.16(17) μ_N^2 and 2.01(25) μ_N^2 for ^{128}Te and ^{130}Te, respectively, which is roughly a factor of five smaller than the calculated strength. However, an adequate comparison between experiment and QPM is not feasible at this point. Due to the low sensitivity of NRF experiments for the inferior $M1$ excitations to the dipole response, decay channels other than from 1^+ states to the ground state usually stay unobserved. Nevertheless, as will be discussed in Sec. IV E, an upper limit of additional $M1$ strength from direct transitions to the 2_1^+ state can be deduced for a few beam energies from coincidence measurements. Regardless of this contribution, a considerable part of the total $M1$ strength is still missed in the experimental analysis due to unobserved decays.

Therefore, additional experiments with complementary probes sensitive to the excitation channel such as inelastic electron [97] and proton scattering [98,99] are necessary to extract the full $M1$ strength for ^{128}Te and ^{130}Te.

D. Primary γ-ray transitions to low-lying levels of ^{128}Te

While photoabsorption and average ground-state transition cross sections yield information on the dipole response built on the ground state, a broader picture of the structure of

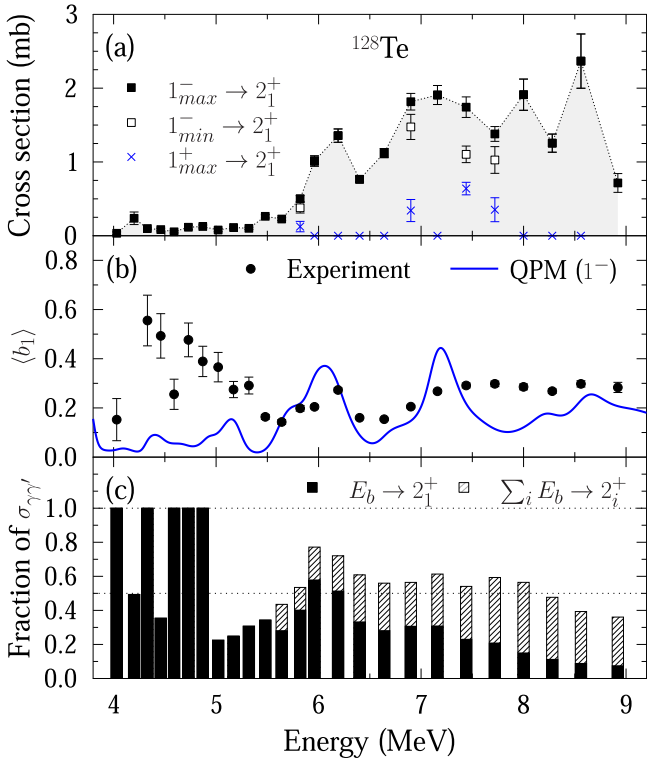

FIG. 18. Balance of experimentally extracted primary γ-ray transitions to low-lying excited states as a function of the beam energy. (a) Complete cross sections for direct population of the 2^+_1 state (black squares). Its separation into parts stemming from 1^- states (open squares) and 1^+ states (blue crosses) will be discussed in more detail in Sec. IV E. (b) Comparison of the average branching ratio $\langle b_1 \rangle$ between experiment (black dots) and QPM calculations for 1^- states (blue line). (c) Analysis of the different relative contributions to $\sigma_{\gamma\gamma'}$ from direct decays to the 2^+_1 state (black bar) and to other low-lying states (shaded bar) including resolved and unresolved transitions.

the PDR is obtained studying its decay behavior. Hence, in the following, a detailed examination of the direct population of low-lying excited states is presented. The analysis of γ-γ coincidences after photo-excitation of nuclear levels of ^{128}Te is applied to γ-ray beam energies from 4 MeV up to 9 MeV in steps of 150 to 350 keV. For all observed primary γ-ray transition channels, the extracted events from LaBr-LaBr coincidences are converted into cross sections for the corresponding reaction channel. The cross sections for the direct population of the 2^+_1 state ($\sigma_{J^\pi \rightarrow 2^+_1} = \sum_x I_{0 \rightarrow x \rightarrow 2^+_1} / \Delta E$) as a function of the excitation energy (black squares) are shown in Fig. 18(a). They vary from 0.25 mb below 6 MeV to about 1–2 mb above 6 MeV. The trend of the cross section as a function of the excitation energy is comparable to the elastic cross sections discussed in Fig. 15(a) in the energy region above 6 MeV, while it deviates at lower excitation energies. This observation becomes more evident scrutinizing the average branching ratio

$$\langle b_1 \rangle = \frac{\sigma_{J^\pi \rightarrow 2^+_1}}{\sigma_{\gamma\gamma}} = \frac{\sum_x I_{0 \rightarrow x \rightarrow 2^+_1}}{\sum_x I_{0 \rightarrow x \rightarrow 0}}, \qquad (14)$$

which describes the fraction of primary transitions to the 2^+_1 relative to the ground-state decay for all individual excited states x in a given excitation-energy window.

Figure 18(b) shows a comparison of the experimental $\langle b_1 \rangle$ values (black dots) to QPM calculations considering the decays from 1^- states (blue solid line). The solid curve is obtained from a moving average of discrete transition widths using a Gaussian distribution with a FWHM corresponding to the spread of the γ-ray beam to imitate the experimental resolution. The data above 5.5 MeV show a reasonable agreement on an absolute scale between experiment and theory for the decay of 1^- states as has been observed before in the case of ^{140}Ce [47], while larger deviations are evident below 5.5 MeV. The experimental data indicate that below an excitation energy of 4.5 MeV the nuclear spectrum is dominated by 1^+ and a few 2^+ levels as outlined in Sec. III C 2, which may impact the observed $\langle b_1 \rangle$ values.

In the present work, the inelastic cross section [$\sigma_{\gamma\gamma'}$, see Eq. (5)] is determined by the total intensity collected in the first (few) excited states; usually the 2^+_1 state. However, it is not clear, whether the 2^+_1 state is predominantly populated via direct transitions from photo-excited states at a given excitation energy or via cascades decaying through intermediate levels. In previous studies, direct [47,100,101] and indirect methods were used to probe the feeding of the 2^+_1, for instance by studying the angular distribution of the observed $2^+_1 \rightarrow 0^+_1$ transition [39,57,102].

The measurement of primary γ-ray transitions allows a direct examination of the individual components that contribute to the inelastic decay channel. In this work, the direct decays to the 2^+_1 and further low-lying levels at energies of up to ≈2.7 MeV are observed for $E_b > 5.5$ MeV. Figure 18(c) shows the different relative contributions to the inelastic cross section $\sigma_{\gamma\gamma'}$. At energies below 5 MeV, the dominant part of $\sigma_{\gamma\gamma'}$ is composed of direct decays to the 2^+_1 state from decay intensities including unresolved transitions ($E_b \rightarrow 2^+_1$, black bars) determined from the analysis of LaBr-LaBr coincidences. Above 5 MeV, the fraction of the inelastic cross section stemming from primary transitions to the 2^+_1 state shows a maximum at around 6 MeV and is decreasing towards higher energies. As the excitation energy increases, decay channels to additional low-lying levels are observed similar to the study with ^{60}Ni [39]. Their summed contribution including all experimentally observed decay channels ($\sum_i E_b \rightarrow 2^+_i$, shaded bars) declines slowly for rising energies being at about 50% of $\sigma_{\gamma\gamma'}$. Thus, the remaining 50% of $\sigma_{\gamma\gamma'}$ consists of many unobserved primaries that populate unknown intermediate levels, partly above 2.7 MeV. This analysis underlines quantitatively the importance of taking the accumulated intensity of low-lying excited states into account to determine $\sigma_{\gamma\gamma'}$ and, thus, the photoabsorption cross sections in experiments with quasimonochromatic γ-ray beams.

In the upcoming section, a method is presented for the distinction between transitions stemming from excited states with different spin-parities. However, the cross sections below 5.5 MeV are an order of magnitude smaller compared to higher excitation energies, wherefore an unambiguous and detailed analysis of the origin of the low-energy enhancement

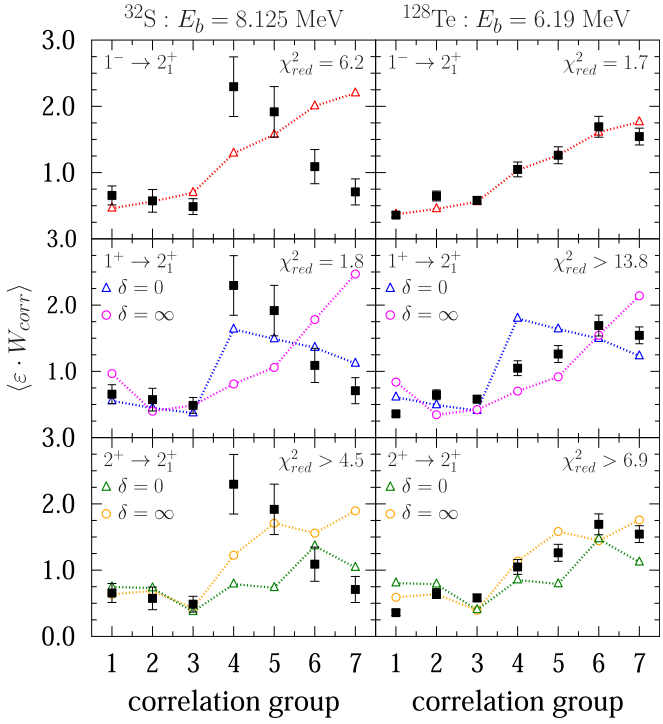

FIG. 19. Angular correlations from γ-γ measurements (black squares) with ^{32}S and its well-known 1^+ state at $E_b = 8.125$ MeV (left-hand side) and exemplarily with ^{128}Te at $E_b = 6.19$ MeV (right-hand side) compared to theoretical values (triangles and circles) grouped into seven correlation groups. For details see text.

of the branching ratio $\langle b_1 \rangle$ is not possible due to the limited statistics in this energy region.

E. Primary transitions to the 2_1^+ level of ^{128}Te

In the following, the measured γ-γ angular correlation is used to extract the dominant character of primary transitions contributing to the direct feeding of the 2_1^+ state. For the correlation between two successively emitted γ-rays, γ_1 and γ_2, the directional distribution function of γ_1 depends on the observation direction of γ_2 (see, e.g., Refs. [86,103]). The available four LaBr detectors of the γ^3 setup were placed at different polar and azimuthal angles (see Table II). Considering the corresponding angular correlations, in total seven γ-γ correlation groups are defined enabling a distinction between the following γ-cascades:

$$0^+ \xrightarrow{\vec{\gamma}_0} 1^- \xrightarrow{\gamma_1} 2^+ \xrightarrow{\gamma_2} 0^+, \tag{15}$$

$$0^+ \xrightarrow{\vec{\gamma}_0} 1^+ \xrightarrow{\gamma_1} 2^+ \xrightarrow{\gamma_2} 0^+, \tag{16}$$

$$0^+ \xrightarrow{\vec{\gamma}_0} 2^+ \xrightarrow{\gamma_1} 2^+ \xrightarrow{\gamma_2} 0^+, \tag{17}$$

where $\vec{\gamma}_0$ indicates the absorption of a γ-ray from the linearly polarized γ-ray beam. The simulated values for each of the considered cascades are shown in Fig. 19, while multipole mixing ratios (following the phase convention of Ref. [104]) of $\delta = 0$ and $\delta = \infty$ are examined as well. The left-hand side of Fig. 19 illustrates the test case of the known $0_1^+ \rightarrow 1^+ \rightarrow 2_1^+ \rightarrow 0_1^+$ cascade of ^{32}S. In ^{32}S, an isolated 1^+ level is located at 8.125 MeV, which has a branching ratio of about 14 % to the 2_1^+ [105]. The best agreement to the experimental data (black squares) is obtained for the angular correlation of a $1^+ \rightarrow 2_1^+$ transition with $\delta = 0$ and a reduced χ^2 of $\chi^2_{\text{red}} = 1.8$, while the other possible cascades cannot describe the data points at all.

In ^{128}Te, different sets of states, i.e., 1^-, 1^+, and 2^+ states, may contribute to the direct population of the 2_1^+ level. As a typical example, an analysis of the different multipole contributions is shown on the right-hand side of Fig. 19 for the measurement with ^{128}Te at $E_b = 6.19$ MeV. The experimental data (black squares) are scaled to the angular correlation values for $1^- \rightarrow 2^+$, $1^+ \rightarrow 2^+$, and $2^+ \rightarrow 2^+$ transitions, respectively. For the given energy, the data are consistent with pure $1^- \rightarrow 2_1^+$ transitions. In the next step, a multipole decomposition analysis (MDA) is applied to the collected data obtained between 5.82 and 8.56 MeV. The experimental data exhibit sufficient counting statistics for an MDA of the measured yields directly populating the 2_1^+ state, while primary γ-ray transitions to higher-lying excited states do not have sufficient statistics. It is noted, that for $E_b <$ 5.82 MeV this analysis is not possible due to the limited statistics.

Figure 18(a) shows the total cross sections for a direct population of the 2_1^+ level (black squares). Since real photons induce predominantly dipole excitations, $1^- \rightarrow 2_1^+$ and $1^+ \rightarrow 2_1^+$ transitions are taken into account in the MDA using multipole mixing ratios of $\delta = 0$ as well as $\delta = \infty$. The results with the minimal χ^2_{red} are shown in Fig. 18(a). The 2_1^+ state is mainly populated by $E1$ transitions, i.e., from 1^- states. For the data obtained at $E_b = 5.82$, 6.9, 7.44, and 7.72 MeV small contributions from deexciting 1^+ states (blue crosses) are observed in addition to $E1$ transitions (open squares). It is noted, that except for $E_b = 7.44$ MeV, the corresponding χ^2_{red} values for these excitation energies are only marginally lower than the ones assuming pure $E1$ character for the population of the 2_1^+ state, which is reflected in the uncertainties of the data points in Fig. 18(a). Conclusively, the obtained cross sections can be considered as upper limits for the part originating from 1^+ states ($1^+_{\text{max}} \rightarrow 2_1^+$) and as lower limits for the contribution from 1^- levels ($1^-_{\text{min}} \rightarrow 2_1^+$) indicated in Fig. 18. Considering these upper limits for the $M1$ transition strength in addition to the fraction from the ground-state decay (as discussed in Sec. IV C), a summed $B(M1) \uparrow$ value of 3.42(28) μ_N^2 is obtained for ^{128}Te between 6.5 MeV and 8.5 MeV, which is still a factor of 2.6 smaller than the expected value of 9 μ_N^2 calculated in the QPM.

The observations for the decay behavior of the $E1$ strength underpin previous experimental results on the mixing of the PDR and the PDR built on top of low-lying states [47]. In Ref. [47], it was assumed that the 2_1^+ of ^{140}Ce is exclusively populated by the PDR states, while in the present study it is verified for ^{128}Te by direct measurements of angular correlations of coincident γ-rays. Furthermore, it will have an impact on the determination of photon strength functions using quasimonochromatic γ-ray beams [27]. In general, it is not trivial to disentangle the involved multipoles in methods exploiting decay γ-ray spectroscopy as done, e.g., in

particle-induced reations (see, e.g., Refs. [22,28,29,106] and references therein). However, the present results show that an MDA in photonuclear reactions with linearly polarized γ-ray beams at the γ^3 setup allows, in principle, for a separation of $E1$ and $M1$ contributions to the measured photon strength function in the deexcitation channel.

V. CONCLUSION

The dipole response in ^{128}Te and ^{130}Te is investigated by photoinduced reactions using bremsstrahlung at the DHIPS as well as by monoenergetic γ-ray beams at the γ^3 setup. A state-by-state analysis and a study of average decay quantities including unresolved transitions reveal a predominant $E1$ character of the dipole strength below the neutron separation threshold of the probed tellurium isotopes. Small contributions of less than $\approx$ 5–10% of the ground-state decays above 5 MeV are attributed to $M1$ transitions. The measured $B(E1)\uparrow$ values of individual transitions as well as the extracted photoabsorption cross sections are in good agreement with calculations within the QPM. In particular, the branching ratio $\langle b_1 \rangle$ to the 2_1^+ state is described reasonably well on an absolute scale by the decay properties of 1^- states above 5.5 MeV. The increasing experimental $\langle b_1 \rangle$ values below that excitation energy are not understood, but may originate from decays of positive-parity states in that energy region. In the present work, however, it is not possible to experimentally confirm that the direct population of the 2_1^+ is driven by 1^+ states below 5.5 MeV. Further studies with enhanced sensitivity are necessary to conclusively resolve this discrepancy. Moreover, it is found that the vast majority of the decays directly populating the 2_1^+ is attributed to $E1$ transitions of the PDR states in the region from 5.82 MeV and 8.56 MeV. Contributions from $M1$ transitions are small compared to the $E1$ part. This observation serves as an additional direct evidence to the results from Ref. [47], that the PDR on the ground state mixes with the PDR built on top of the 2_1^+. Furthermore, an analysis of the inelastic cross section $\sigma_{\gamma\gamma'}$ that is extracted from the total population intensity of the 2_1^+ state shows that about half of its cross section is due to primary γ-ray transitions populating low-lying levels below 2.7 MeV. Thus, the second half is increasingly dominated by cascade decays via unknown intermediate levels located at energies above 2.7 MeV.

The presented work emphasizes the paramount advantage of monochromatic γ-ray beams in combination with a γ-γ coincidence setup for the model-independent determination of photoabsorption cross sections and the decay behavior of the dipole strength below the particle thresholds. Experiments with an enhanced sensitivity to weak decay branchings are under way to deepen the investigation of the decay behavior of photo-excited states in the PDR region at HIγS. It will be possible to not only study in detail the decay character of primary transitions populating the 2_1^+, but extend the research to further low-lying excited states.

ACKNOWLEDGMENTS

The authors thank the S-DALINAC operating team and the HIγS accelerator staff for providing excellent γ-ray beams and experimental conditions. This work was supported by the Deutsche Forschungsgemeinschaft (DFG, German Research Foundation) - Project-ID 279384907 - SFB 1245, by the State of Hesse under grant "Nuclear Photonics" within the LOEWE program, by BMBF (Grant No. 05P18RDEN9), and by the U.S Department of Energy, Office of Nuclear Physics under Grant No. DE-FG02-97ER41033. M.S. acknowledges financial support by the STFC (Grant No ST/P005101/1).

[1] W. Bothe and W. Gentner, Z. Phys. **106**, 236 (1937).
[2] G. C. Baldwin and G. S. Klaiber, Phys. Rev. **71**, 3 (1947).
[3] P. Bortignon, A. Bracco, and R. Broglia, *Giant Resonances: Nuclear Structure at Finite Temperature* (Harwood Academic Publishers, Reading, UK, 1998).
[4] M. N. Harakeh and A. van der Woude, *Giant Resonances: Fundamental High-Frequency Modes of Nuclear Excitation* (Oxford University Press, Oxford, UK, 2001).
[5] A. Migdal, J. Phys. (USSR) **8**, 331 (1944).
[6] G. A. Bartholomew, Annu. Rev. Nucl. Sci. **11**, 259 (1961).
[7] G. A. Bartholomew, E. D. Earle, A. J. Ferguson, J. W. Knowles, and M. A. Lone, Adv. Nucl. Phys. **7**, 229 (1973).
[8] D. Savran, T. Aumann, and A. Zilges, Prog. Part. Nucl. Phys. **70**, 210 (2013).
[9] A. Bracco, F. C. L. Crespi, and E. G. Lanza, Eur. Phys. J. A **51**, 99 (2015).
[10] A. Bracco, E. G. Lanza, and A. Tamii, Prog. Part. Nucl. Phys. **106**, 360 (2019).
[11] R. Mohan, M. Danos, and L. C. Biedenharn, Phys. Rev. C **3**, 1740 (1971).
[12] E. G. Lanza, A. Vitturi, and M. V. Andrés, Phys. Rev. C **91**, 054607 (2015).
[13] S. F. Semenko, Sov. J. Nucl. Phys. **34**, 356 (1981).
[14] A. Repko, V. O. Nesterenko, J. Kvasil, and P.-G. Reinhard, Eur. Phys. J. A **55**, 242 (2019).
[15] S. Goriely, Phys. Lett. B **436**, 10 (1998).
[16] S. Goriely, E. Khan, and M. Samyn, Nucl. Phys. A **739**, 331 (2004).
[17] H. Utsunomiya, S. Goriely, M. Kamata, T. Kondo, O. Itoh, H. Akimune, T. Yamagata, H. Toyokawa, Y. W. Lui, S. Hilaire, and A. J. Koning, Phys. Rev. C **80**, 055806 (2009).
[18] I. Daoutidis and S. Goriely, Phys. Rev. C **86**, 034328 (2012).
[19] A. Tonchev, N. Tsoneva, C. Bhatia, C. Arnold, S. Goriely, S. Hammond, J. Kelley, E. Kwan, H. Lenske, J. Piekarewicz, R. Raut, G. Rusev, T. Shizuma, and W. Tornow, Phys. Lett. B **773**, 20 (2017).
[20] M. Krtička, F. Bečvář, J. Honzátko, I. Tomandl, M. Heil, F. Käppeler, R. Reifarth, F. Voss, and K. Wisshak, Phys. Rev. Lett. **92**, 172501 (2004).
[21] R. Schwengner, G. Rusev, N. Tsoneva, N. Benouaret, R. Beyer, M. Erhard, E. Grosse, A. R. Junghans, J. Klug, K. Kosev, H. Lenske, C. Nair, K. D. Schilling, and A. Wagner, Phys. Rev. C **78**, 064314 (2008).

[22] M. Wiedeking, L. A. Bernstein, M. Krtička, D. L. Bleuel, J. M. Allmond, M. S. Basunia, J. T. Burke, P. Fallon, R. B. Firestone, B. L. Goldblum, R. Hatarik, P. T. Lake, I.-Y. Lee, S. R. Lesher, S. Paschalis, M. Petri, L. Phair, and N. D. Scielzo, Phys. Rev. Lett. **108**, 162503 (2012).

[23] J. Isaak, D. Savran, M. Krtička, M. Ahmed, J. Beller, E. Fiori, J. Glorius, J. Kelley, B. Löher, N. Pietralla, C. Romig, G. Rusev, M. Scheck, L. Schnorrenberger, J. Silva, K. Sonnabend, A. Tonchev, W. Tornow, H. Weller, and M. Zweidinger, Phys. Lett. B **727**, 361 (2013).

[24] J. L. Ullmann, T. Kawano, T. A. Bredeweg, A. Couture, R. C. Haight, M. Jandel, J. M. O'Donnell, R. S. Rundberg, D. J. Vieira, J. B. Wilhelmy, J. A. Becker, A. Chyzh, C. Y. Wu, B. Baramsai, G. E. Mitchell, and M. Krtička, Phys. Rev. C **89**, 034603 (2014).

[25] A. Spyrou, S. N. Liddick, A. C. Larsen, M. Guttormsen, K. Cooper, A. C. Dombos, D. J. Morrissey, F. Naqvi, G. Perdikakis, S. J. Quinn, T. Renstrøm, J. A. Rodriguez, A. Simon, C. S. Sumithrarachchi, and R. G. T. Zegers, Phys. Rev. Lett. **113**, 232502 (2014).

[26] M. Guttormsen, A. C. Larsen, A. Görgen, T. Renstrøm, S. Siem, T. G. Tornyi, and G. M. Tveten, Phys. Rev. Lett. **116**, 012502 (2016).

[27] J. Isaak, D. Savran, B. Löher, T. Beck, M. Bhike, U. Gayer, Krishichayan, N. Pietralla, M. Scheck, W. Tornow, V. Werner, A. Zilges, and M. Zweidinger, Phys. Lett. B **788**, 225 (2019).

[28] S. Goriely, P. Dimitriou, M. Wiedeking, T. Belgya, R. Firestone, J. Kopecky, M. Krtička, V. Plujko, R. Schwengner, S. Siem, H. Utsunomiya, S. Hilaire, S. Péru, Y. S. Cho, D. M. Filipescu, N. Iwamoto, T. Kawano, V. Varlamov, and R. Xu, Eur. Phys. J. A **55**, 172 (2019).

[29] A. Larsen, A. Spyrou, S. Liddick, and M. Guttormsen, Prog. Part. Nucl. Phys. **107**, 69 (2019).

[30] J. Wilhelmy, M. Müscher, G. Rusev, R. Schwengner, R. Beyer, M. Bhike, P. Erbacher, F. Fiedler, U. Friman-Gayer, J. Glorius, R. Greifenhagen, S. Hammer, T. Hensel, J. Isaak, A. R. Junghans, Krishichayan, B. Löher, S. E. Müller, N. Pietralla, S. Reinicke, D. Savran, P. Scholz, K. Sonnabend, T. Szücs, M. Tamkas, W. Tornow, S. Turkat, A. Wagner, and A. Zilges, Phys. Rev. C **102**, 044327 (2020).

[31] W. Hauser and H. Feshbach, Phys. Rev. **87**, 366 (1952).

[32] A. Koning, *Nuclear Data for Science and Technology*, edited by O. Bersillon, F. Gunsing, E. Bauge, R. Jacqmin, and S. Leray (EDP Sciences, Les Ulis, France, 2008) p. 211.

[33] M. Herman, R. Capote, B. Carlson, P. Obložinský, M. Sin, A. Trkov, H. Wienke, and V. Zerkin, Nucl. Data Sheets **108**, 2655 (2007).

[34] T. Hartmann, M. Babilon, S. Kamerdzhiev, E. Litvinova, D. Savran, S. Volz, and A. Zilges, Phys. Rev. Lett. **93**, 192501 (2004).

[35] J. Isaak, D. Savran, M. Fritzsche, D. Galaviz, T. Hartmann, S. Kamerdzhiev, J. H. Kelley, E. Kwan, N. Pietralla, C. Romig, G. Rusev, K. Sonnabend, A. P. Tonchev, W. Tornow, and A. Zilges, Phys. Rev. C **83**, 034304 (2011).

[36] H. Pai, J. Beller, N. Benouaret, J. Enders, T. Hartmann, O. Karg, P. von Neumann-Cosel, N. Pietralla, V. Y. Ponomarev, C. Romig, M. Scheck, L. Schnorrenberger, S. Volz, and M. Zweidinger, Phys. Rev. C **88**, 054316 (2013).

[37] J. Wilhelmy, B. A. Brown, P. Erbacher, U. Gayer, J. Isaak, Krishichayan, B. Löher, M. Müscher, H. Pai, N. Pietralla, P. Ries, D. Savran, P. Scholz, M. Spieker, W. Tornow, V. Werner, and A. Zilges, Phys. Rev. C **98**, 034315 (2018).

[38] P. C. Ries, H. Pai, T. Beck, J. Beller, M. Bhike, V. Derya, U. Gayer, J. Isaak, B. Löher, Krishichayan, L. Mertes, N. Pietralla, C. Romig, D. Savran, M. Schilling, W. Tornow, S. Typel, V. Werner, J. Wilhelmy, A. Zilges, and M. Zweidinger, Phys. Rev. C **100**, 021301(R) (2019).

[39] M. Scheck, V. Y. Ponomarev, T. Aumann, J. Beller, M. Fritzsche, J. Isaak, J. H. Kelley, E. Kwan, N. Pietralla, R. Raut, C. Romig, G. Rusev, D. Savran, K. Sonnabend, A. P. Tonchev, W. Tornow, H. R. Weller, and M. Zweidinger, Phys. Rev. C **87**, 051304(R) (2013).

[40] M. Scheck, V. Y. Ponomarev, M. Fritzsche, J. Joubert, T. Aumann, J. Beller, J. Isaak, J. H. Kelley, E. Kwan, N. Pietralla, R. Raut, C. Romig, G. Rusev, D. Savran, L. Schorrenberger, K. Sonnabend, A. P. Tonchev, W. Tornow, H. R. Weller, A. Zilges, and M. Zweidinger, Phys. Rev. C **88**, 044304 (2013).

[41] O. Wieland, A. Bracco, F. Camera, G. Benzoni, N. Blasi, S. Brambilla, F. C. L. Crespi, S. Leoni, B. Million, R. Nicolini, A. Maj, P. Bednarczyk, J. Grebosz, M. Kmiecik, W. Meczynski, J. Styczen, T. Aumann, A. Banu, T. Beck, F. Becker, L. Caceres, P. Doornenbal, H. Emling, J. Gerl, H. Geissel, M. Gorska, O. Kavatsyuk, M. Kavatsyuk, I. Kojouharov, N. Kurz, R. Lozeva, N. Saito, T. Saito, H. Schaffner, H. J. Wollersheim, J. Jolie, P. Reiter, N. Warr, G. deAngelis, A. Gadea, D. Napoli, S. Lenzi, S. Lunardi, D. Balabanski, G. LoBianco, C. Petrache, A. Saltarelli, M. Castoldi, A. Zucchiatti, J. Walker, and A. Bürger, Phys. Rev. Lett. **102**, 092502 (2009).

[42] D. M. Rossi, P. Adrich, F. Aksouh, H. Alvarez-Pol, T. Aumann, J. Benlliure, M. Böhmer, K. Boretzky, E. Casarejos, M. Chartier, A. Chatillon, D. Cortina-Gil, U. Datta Pramanik, H. Emling, O. Ershova, B. Fernandez-Dominguez, H. Geissel, M. Gorska, M. Heil, H. T. Johansson, A. Junghans, A. Kelic-Heil, O. Kiselev, A. Klimkiewicz, J. V. Kratz, R. Krücken, N. Kurz, M. Labiche, T. Le Bleis, R. Lemmon, Y. A. Litvinov, K. Mahata, P. Maierbeck, A. Movsesyan, T. Nilsson, C. Nociforo, R. Palit, S. Paschalis, R. Plag, R. Reifarth, D. Savran, H. Scheit, H. Simon, K. Sümmerer, A. Wagner, W. Waluś, H. Weick, and M. Winkler, Phys. Rev. Lett. **111**, 242503 (2013).

[43] O. Wieland, A. Bracco, F. Camera, R. Avigo, H. Baba, N. Nakatsuka, T. Aumann, S. R. Banerjee, G. Benzoni, K. Boretzky, C. Caesar, S. Ceruti, S. Chen, F. C. L. Crespi, V. Derya, P. Doornenbal, N. Fukuda, A. Giaz, K. Ieki, N. Kobayashi, Y. Kondo, S. Koyama, T. Kubo, M. Matsushita, B. Million, T. Motobayashi, T. Nakamura, M. Nishimura, H. Otsu, T. Ozaki, A. T. Saito, H. Sakurai, H. Scheit, F. Schindler, P. Schrock, Y. Shiga, M. Shikata, S. Shimoura, D. Steppenbeck, T. Sumikama, S. Takeuchi, R. Taniuchi, Y. Togano, J. Tscheuschner, J. Tsubota, H. Wang, K. Wimmer, and K. Yoneda, Phys. Rev. C **98**, 064313 (2018).

[44] A. Zilges, S. Volz, M. Babilon, T. Hartmann, P. Mohr, and K. Vogt, Phys. Lett. B **542**, 43 (2002).

[45] S. Volz, N. Tsoneva, M. Babilon, M. Elvers, J. Hasper, R.-D. Herzberg, H. Lenske, K. Lindenberg, D. Savran, and A. Zilges, Nucl. Phys. A **779**, 1 (2006).

[46] D. Savran, M. Fritzsche, J. Hasper, K. Lindenberg, S. Müller, V. Y. Ponomarev, K. Sonnabend, and A. Zilges, Phys. Rev. Lett. **100**, 232501 (2008).

[47] B. Löher, D. Savran, T. Aumann, J. Beller, M. Bhike, N. Cooper, V. Derya, M. Duchêne, J. Endres, A. Hennig, P. Humby, J. Isaak, J. Kelley, M. Knörzer, N. Pietralla, V.

Ponomarev, C. Romig, M. Scheck, H. Scheit, J. Silva, A. Tonchev, W. Tornow, F. Wamers, H. Weller, V. Werner, and A. Zilges, Phys. Lett. B **756**, 72 (2016).

[48] K. Govaert, F. Bauwens, J. Bryssinck, D. De Frenne, E. Jacobs, W. Mondelaers, L. Govor, and V. Y. Ponomarev, Phys. Rev. C **57**, 2229 (1998).

[49] J. Endres, E. Litvinova, D. Savran, P. A. Butler, M. N. Harakeh, S. Harissopulos, R.-D. Herzberg, R. Krücken, A. Lagoyannis, N. Pietralla, V. Y. Ponomarev, L. Popescu, P. Ring, M. Scheck, K. Sonnabend, V. I. Stoica, H. J. Wörtche, and A. Zilges, Phys. Rev. Lett. **105**, 212503 (2010).

[50] B. Özel-Tashenov, J. Enders, H. Lenske, A. M. Krumbholz, E. Litvinova, P. von Neumann-Cosel, I. Poltoratska, A. Richter, G. Rusev, D. Savran, and N. Tsoneva, Phys. Rev. C **90**, 024304 (2014).

[51] A. Krumbholz, P. von Neumann-Cosel, T. Hashimoto, A. Tamii, T. Adachi, C. Bertulani, H. Fujita, Y. Fujita, E. Ganioglu, K. Hatanaka, C. Iwamoto, T. Kawabata, N. Khai, A. Krugmann, D. Martin, H. Matsubara, R. Neveling, H. Okamura, H. Ong, I. Poltoratska, V. Ponomarev, A. Richter, H. Sakaguchi, Y. Shimbara, Y. Shimizu, J. Simonis, F. Smit, G. Susoy, J. Thies, T. Suzuki, M. Yosoi, and J. Zenihiro, Phys. Lett. B **744**, 7 (2015).

[52] M. Müscher, J. Wilhelmy, R. Massarczyk, R. Schwengner, M. Grieger, J. Isaak, A. R. Junghans, T. Kögler, F. Ludwig, D. Savran, D. Symochko, M. P. Takács, M. Tamkas, A. Wagner, and A. Zilges, Phys. Rev. C **102**, 014317 (2020).

[53] S. Bassauer, P. von Neumann-Cosel, P.-G. Reinhard, A. Tamii, S. Adachi, C. A. Bertulani, P. Y. Chan, A. D'Alessio, H. Fujioka, H. Fujita, Y. Fujita, G. Gey, M. Hilcker, T. H. Hoang, A. Inoue, J. Isaak, C. Iwamoto, T. Klaus, N. Kobayashi, Y. Maeda, M. Matsuda, N. Nakatsuka, S. Noji, H. J. Ong, I. Ou, N. Pietralla, V. Y. Ponomarev, M. S. Reen, A. Richter, M. Singer, G. Steinhilber, T. Sudo, Y. Togano, M. Tsumura, Y. Watanabe, and V. Werner, Phys. Rev. C **102**, 034327 (2020).

[54] S. Bassauer, P. von Neumann-Cosel, P.-G. Reinhard, A. Tamii, S. Adachi, C. Bertulani, P. Chan, G. Colò, A. D'Alessio, H. Fujioka, H. Fujita, Y. Fujita, G. Gey, M. Hilcker, T. Hoang, A. Inoue, J. Isaak, C. Iwamoto, T. Klaus, N. Kobayashi, Y. Maeda, M. Matsuda, N. Nakatsuka, S. Noji, H. Ong, I. Ou, N. Paar, N. Pietralla, V. Ponomarev, M. Reen, A. Richter, X. Roca-Maza, M. Singer, G. Steinhilber, T. Sudo, Y. Togano, M. Tsumura, Y. Watanabe, and V. Werner, Phys. Lett. B **810**, 135804 (2020).

[55] P. Adrich, A. Klimkiewicz, M. Fallot, K. Boretzky, T. Aumann, D. Cortina-Gil, U. Datta Pramanik, Th. W. Elze, H. Emling, H. Geissel, M. Hellström, K. L. Jones, J. V. Kratz, R. Kulessa, Y. Leifels, C. Nociforo, R. Palit, H. Simon, G. Surówka, K. Sümmerer, and W. Waluś, Phys. Rev. Lett. **95**, 132501 (2005).

[56] A. Klimkiewicz, N. Paar, P. Adrich, M. Fallot, K. Boretzky, T. Aumann, D. Cortina-Gil, U. Datta Pramanik, Th. W. Elze, H. Emling, H. Geissel, M. Hellström, K. L. Jones, J. V. Kratz, R. Kulessa, C. Nociforo, R. Palit, H. Simon, G. Surówka, K. Sümmerer, D. Vretenar, and W. Waluś, Phys. Rev. C **76**, 051603(R) (2007).

[57] C. Romig, J. Beller, J. Glorius, J. Isaak, J. H. Kelley, E. Kwan, N. Pietralla, V. Y. Ponomarev, A. Sauerwein, D. Savran, M. Scheck, L. Schnorrenberger, K. Sonnabend, A. P. Tonchev, W. Tornow, H. R. Weller, A. Zilges, and M. Zweidinger, Phys. Rev. C **88**, 044331 (2013).

[58] G. Rusev, R. Schwengner, F. Dönau, M. Erhard, E. Grosse, A. R. Junghans, K. Kosev, K. D. Schilling, A. Wagner, F. Bečvář, and M. Krtička, Phys. Rev. C **77**, 064321 (2008).

[59] G. Rusev, R. Schwengner, R. Beyer, M. Erhard, E. Grosse, A. R. Junghans, K. Kosev, C. Nair, K. D. Schilling, A. Wagner, F. Dönau, and S. Frauendorf, Phys. Rev. C **79**, 061302(R) (2009).

[60] D. Martin, P. von Neumann-Cosel, A. Tamii, N. Aoi, S. Bassauer, C. A. Bertulani, J. Carter, L. Donaldson, H. Fujita, Y. Fujita, T. Hashimoto, K. Hatanaka, T. Ito, A. Krugmann, B. Liu, Y. Maeda, K. Miki, R. Neveling, N. Pietralla, I. Poltoratska, V. Y. Ponomarev, A. Richter, T. Shima, T. Yamamoto, and M. Zweidinger, Phys. Rev. Lett. **119**, 182503 (2017).

[61] N. Ryezayeva, T. Hartmann, Y. Kalmykov, H. Lenske, P. von Neumann-Cosel, V. Y. Ponomarev, A. Richter, A. Shevchenko, S. Volz, and J. Wambach, Phys. Rev. Lett. **89**, 272502 (2002).

[62] T. Shizuma, N. Iwamoto, A. Makinaga, R. Massarczyk, R. Schwengner, R. Beyer, D. Bemmerer, M. Dietz, A. Junghans, T. Kögler, F. Ludwig, S. Reinicke, S. Schulz, S. Urlaß, and A. Wagner, Phys. Rev. C **98**, 064317 (2018).

[63] D. Savran, M. Babilon, A. M. van den Berg, M. N. Harakeh, J. Hasper, A. Matic, H. J. Wörtche, and A. Zilges, Phys. Rev. Lett. **97**, 172502 (2006).

[64] V. Derya, D. Savran, J. Endres, M. Harakeh, H. Hergert, J. Kelley, P. Papakonstantinou, N. Pietralla, V. Ponomarev, R. Roth, G. Rusev, A. Tonchev, W. Tornow, H. Wörtche, and A. Zilges, Phys. Lett. B **730**, 288 (2014).

[65] D. Savran, V. Derya, S. Bagchi, J. Endres, M. Harakeh, J. Isaak, N. Kalantar-Nayestanaki, E. Lanza, B. Löher, A. Najafi, S. Pascu, S. Pickstone, N. Pietralla, V. Ponomarev, C. Rigollet, C. Romig, M. Spieker, A. Vitturi, and A. Zilges, Phys. Lett. B **786**, 16 (2018).

[66] L. Pellegri, A. Bracco, F. Crespi, S. Leoni, F. Camera, E. Lanza, M. Kmiecik, A. Maj, R. Avigo, G. Benzoni, N. Blasi, C. Boiano, S. Bottoni, S. Brambilla, S. Ceruti, A. Giaz, B. Million, A. Morales, R. Nicolini, V. Vandone, O. Wieland, D. Bazzacco, P. Bednarczyk, M. Bellato, B. Birkenbach, D. Bortolato, B. Cederwall, L. Charles, M. Ciemala, G. D. Angelis, P. Désesquelles, J. Eberth, E. Farnea, A. Gadea, R. Gernhäuser, A. Görgen, A. Gottardo, J. Grebosz, H. Hess, R. Isocrate, J. Jolie, D. Judson, A. Jungclaus, N. Karkour, M. Krzysiek, E. Litvinova, S. Lunardi, K. Mazurek, D. Mengoni, C. Michelagnoli, R. Menegazzo, P. Molini, D. Napoli, A. Pullia, B. Quintana, F. Recchia, P. Reiter, M. Salsac, B. Siebeck, S. Siem, J. Simpson, P.-A. Söderström, O. Stezowski, C. Theisen, C. Ur, J. V. Dobon, and M. Zieblinski, Phys. Lett. B **738**, 519 (2014).

[67] F. C. L. Crespi, A. Bracco, R. Nicolini, D. Mengoni, L. Pellegri, E. G. Lanza, S. Leoni, A. Maj, M. Kmiecik, R. Avigo, G. Benzoni, N. Blasi, C. Boiano, S. Bottoni, S. Brambilla, F. Camera, S. Ceruti, A. Giaz, B. Million, A. I. Morales, V. Vandone, O. Wieland, P. Bednarczyk, M. Ciemała, J. Grebosz, M. Krzysiek, K. Mazurek, M. Zieblinski, D. Bazzacco, M. Bellato, B. Birkenbach, D. Bortolato, E. Calore, B. Cederwall, L. Charles, G. de Angelis, P. Désesquelles, J. Eberth, E. Farnea, A. Gadea, A. Görgen, A. Gottardo, R. Isocrate, J. Jolie, A. Jungclaus, N. Karkour, W. Korten, R. Menegazzo, C. Michelagnoli, P. Molini, D. R. Napoli, A. Pullia, F. Recchia, P. Reiter, D. Rosso, E. Sahin, M. D. Salsac, B. Siebeck, S. Siem,

J. Simpson, P.-A. Söderström, O. Stezowski, C. Theisen, C. Ur, and J. J. Valiente-Dobón, Phys. Rev. Lett. **113**, 012501 (2014).
[68] M. Scheck, S. Mishev, V. Y. Ponomarev, R. Chapman, L. P. Gaffney, E. T. Gregor, N. Pietralla, P. Spagnoletti, D. Savran, and G. S. Simpson, Phys. Rev. Lett. **116**, 132501 (2016).
[69] K. Mashtakov, V. Ponomarev, M. Scheck, S. Finch, J. Isaak, M. Zweidinger, O. Agar, C. Bathia, T. Beck, J. Beller, M. Bowry, R. Chapman, M. Chisthi, U. Friman-Gayer, L. Gaffney, P. Garrett, E. Gregor, J. Keatings, U. Köster, B. Löher, A. McLean, D. O'Donnell, H. Pai, N. Pietralla, G. Rainovski, M. Ramdhane, C. Romig, G. Rusev, D. Savran, G. Simpson, J. Sinclair, K. Sonnabend, P. Spagnoletti, A. Tonchev, and W. Tornow, arXiv:2003.11572.
[70] F. R. Metzger, Prog. in Nucl. Phys. **7**, 53 (1959).
[71] U. Kneissl, H. H. Pitz, and A. Zilges, Prog. Part. Nucl. Phys. **37**, 349 (1996).
[72] U. Kneissl, N. Pietralla, and A. Zilges, J. Phys. G **32**, R217 (2006).
[73] B. Löher, V. Derya, T. Aumann, J. Beller, N. Cooper, M. Duchêne, J. Endres, E. Fiori, J. Isaak, J. Kelley, M. Knörzer, N. Pietralla, C. Romig, D. Savran, M. Scheck, H. Scheit, J. Silva, A. Tonchev, W. Tornow, H. Weller, V. Werner, and A. Zilges, Nucl. Instr. and Meth. A **723**, 136 (2013).
[74] V. G. Soloviev, *Theory of Atomic Nuclei: Quasiparticles and Phonons* (Institute of Physics, Bristol, 1992).
[75] See Supplemental Material at http://link.aps.org/supplemental/10.1103/PhysRevC.103.044317 for tabulated experimental data presented in this article. Already known properties of some nuclear levels are taken from Refs. [76–80].
[76] Z. Elekes and J. Timar, Nucl. Data Sheets **129**, 191 (2015).
[77] S. F. Hicks, J. C. Boehringer, N. Boukharouba, C. Fransen, S. R. Lesher, J. M. Mueller, J. R. Vanhoy, and S. W. Yates, Phys. Rev. C **86**, 054308 (2012).
[78] R. Schwengner, G. Winter, W. Schauer, M. Grinberg, F. Becker, P. von Brentano, J. Eberth, J. Enders, T. von Egidy, R.-D. Herzberg, N. Huxel, L. Kübler, P. von Neumann-Cosel, N. Nicolay, J. Ott, N. Pietralla, H. Prade, S. Raman, J. Reif, A. Richter, C. Schlegel, H. Schnare, T. Servene, S. Skoda, T. Steinhardt, C. Stoyanov, H. Thomas, I. Wiedenhöver, and A. Zilges, Nucl. Phys. A **620**, 277 (1997).
[79] R. Schwengner, G. Winter, W. Schauer, M. Grinberg, F. Becker, P. von Brentano, J. Eberth, J. Enders, T. von Egidy, R.-D. Herzberg, N. Huxel, L. Kübler, P. von Neumann-Cosel, N. Nicolay, J. Ott, N. Pietralla, H. Prade, S. Raman, J. Reif, A. Richter, C. Schlegel, H. Schnare, T. Servene, S. Skoda, T. Steinhardt, C. Stoyanov, H. Thomas, I. Wiedenhöver, and A. Zilges, Nucl. Phys. A **624**, 776 (1997).
[80] B. Singh, Nucl. Data Sheets **93**, 33 (2001).
[81] K. Sonnabend, D. Savran, J. Beller, M. Büssing, A. Constantinescu, M. Elvers, J. Endres, M. Fritzsche, J. Glorius, J. Hasper, J. Isaak, B. Löher, S. Müller, N. Pietralla, C. Romig, A. Sauerwein, L. Schnorrenberger, C. Wälzlein, A. Zilges, and M. Zweidinger, Nucl. Instr. and Meth. A **640**, 6 (2011).
[82] N. Pietralla, Nuclear Physics News **28**, 4 (2018).
[83] T. J. Paulus and R. M. Keyser, Nucl. Instr. Meth. A **286**, 364 (1990).
[84] H. R. Weller, M. W. Ahmed, H. Gao, W. Tornow, Y. K. Wu, M. Gai, and R. Miskimen, Prog. Part. Nucl. Phys. **62**, 257 (2009).
[85] B. Löher, Probing the Decay Characteristics of the Pygmy Dipole Resonance in the Semi-Magic Nucleus ^{140}Ce with γ-γ Coincidence Measurements, Ph.D. thesis, Johannes Gutenberg-Universität Mainz (2014).
[86] J. Isaak, Investigation of decay properties of the Pygmy Dipole Resonance and photon strength functions on excited states in $(\vec{\gamma}, \gamma'\gamma'')$ reactions, Ph.D. thesis, Johannes Gutenberg-Universität Mainz (2016).
[87] J. Kelley, E. Kwan, J. Purcell, C. Sheu, and H. Weller, Nucl. Phys. A **880**, 88 (2012).
[88] R. Schwengner, G. Rusev, N. Benouaret, R. Beyer, M. Erhard, E. Grosse, A. R. Junghans, J. Klug, K. Kosev, L. Kostov, C. Nair, N. Nankov, K. D. Schilling, and A. Wagner, Phys. Rev. C **76**, 034321 (2007).
[89] A. P. Tonchev, S. L. Hammond, J. H. Kelley, E. Kwan, H. Lenske, G. Rusev, W. Tornow, and N. Tsoneva, Phys. Rev. Lett. **104**, 072501 (2010).
[90] N. Pietralla, Z. Berant, V. N. Litvinenko, S. Hartman, F. F. Mikhailov, I. V. Pinayev, G. Swift, M. W. Ahmed, J. H. Kelley, S. O. Nelson, R. Prior, K. Sabourov, A. P. Tonchev, and H. R. Weller, Phys. Rev. Lett. **88**, 012502 (2001).
[91] C. Romig, D. Savran, J. Beller, J. Birkhan, A. Endres, M. Fritzsche, J. Glorius, J. Isaak, N. Pietralla, M. Scheck, L. Schnorrenberger, K. Sonnabend, and M. Zweidinger, Phys. Lett. B **744**, 369 (2015).
[92] D. Savran, M. Elvers, J. Endres, M. Fritzsche, B. Löher, N. Pietralla, V. Y. Ponomarev, C. Romig, L. Schnorrenberger, K. Sonnabend, and A. Zilges, Phys. Rev. C **84**, 024326 (2011).
[93] J. Endres, D. Savran, A. M. van den Berg, P. Dendooven, M. Fritzsche, M. N. Harakeh, J. Hasper, H. J. Wörtche, and A. Zilges, Phys. Rev. C **80**, 034302 (2009).
[94] A. Leprêtre, H. Beil, R. Bergère, P. Carlos, J. Fagot, A. de Miniac, A. Veyssière, and H. Miyase, Nucl. Phys. A **258**, 350 (1976).
[95] W. Kuhn, Z. Phys. **33**, 408 (1925).
[96] F. Reiche and W. Thomas, Z. Phys. **34**, 510 (1925).
[97] K. Heyde, P. von Neumann-Cosel, and A. Richter, Rev. Mod. Phys. **82**, 2365 (2010).
[98] P. von Neumann-Cosel and A. Tamii, Eur. Phys. J. A **55**, 110 (2019).
[99] J. Birkhan, H. Matsubara, P. von Neumann-Cosel, N. Pietralla, V. Y. Ponomarev, A. Richter, A. Tamii, and J. Wambach, Phys. Rev. C **93**, 041302(R) (2016).
[100] M. Tamkas, E. Açıksöz, J. Isaak, T. Beck, N. Benouaret, M. Bhike, I. Boztosun, A. Durusoy, U. Gayer, Krishichayan, B. Löher, N. Pietralla, D. Savran, W. Tornow, V. Werner, A. Zilges, and M. Zweidinger, Nucl. Phys. A **987**, 79 (2019).
[101] O. Papst, V. Werner, J. Isaak, N. Pietralla, T. Beck, C. Bernards, M. Bhike, N. Cooper, B. P. Crider, U. Friman-Gayer, J. Kleemann, Krishichayan, B. Löher, F. Naqvi, E. E. Peters, F. M. Prados-Estévez, R. S. Ilieva, T. J. Ross, D. Savran, W. Tornow, and J. R. Vanhoy, Phys. Rev. C **102**, 034323 (2020).
[102] U. Gayer, T. Beck, M. Bhike, J. Isaak, N. Pietralla, P. C. Ries, D. Savran, M. Schilling, W. Tornow, and V. Werner, Phys. Rev. C **100**, 034305 (2019).
[103] R. M. Steffen and K. Alder, in *The Electromagnetic Interaction in Nuclear Spectroscopy*, edited by W. D. Hamilton (North-Holland Publishing Co., Amsterdam, 1975), Chap. 12, pp. 505–582.
[104] K. Krane, R. Steffen, and R. Wheeler, At. Data Nucl. Data Tables **11**, 351 (1973).

[105] C. Ouellet and B. Singh, Nucl. Data Sheets **112**, 2199 (2011).

[106] M. D. Jones, A. O. Macchiavelli, M. Wiedeking, L. A. Bernstein, H. L. Crawford, C. M. Campbell, R. M. Clark, M. Cromaz, P. Fallon, I. Y. Lee, M. Salathe, A. Wiens, A. D. Ayangeakaa, D. L. Bleuel, S. Bottoni, M. P. Carpenter, H. M. Davids, J. Elson, A. Görgen, M. Guttormsen, R. V. F. Janssens, J. E. Kinnison, L. Kirsch, A. C. Larsen, T. Lauritsen, W. Reviol, D. G. Sarantites, S. Siem, A. V. Voinov, and S. Zhu, Phys. Rev. C **97**, 024327 (2018).